
Article:

Clark, PA, Browning, KA, Forbes, RM et al. (2014) The evolution of an MCS over southern England. Part 2: Model simulations and sensitivity to microphysics. Quarterly Journal of the Royal Meteorological Society, 140 (679). 458 - 479. ISSN: 0035-9009

https://doi.org/10.1002/qj.2142

Quarterly Journal of the Royal Meteorological Society *Q. J. R. Meteorol. Soc.* 140: 458–479, January 2014 B

The evolution of an MCS over southern England. Part 2: Model simulations and sensitivity to microphysics

P. A. Clark,*[a] K. A. Browning,[a] R. M. Forbes,[b] C. J. Morcrette,[c†]
A. M. Blyth[d] and H. W. Lean[e†]
[a]*Department of Meteorology, University of Reading, UK*
[b]*ECMWF, Reading, UK*
[c]*Met Office, Exeter, UK*
[d]*School of Earth and Environment, University of Leeds, UK*
[e]*MetOffice@Reading, Met Office, Reading, UK*
*Correspondence to: P. A. Clark, Department of Meteorology, University of Reading, PO Box 243, Earley Gate, Reading RG6 6BB, Berkshire, UK. E-mail: p.clark@reading.ac.uk
†The contributions of these authors were written in the course of their employment at the Met Office, UK and are published with the permission of the Controller of HMSO and the Queen's Printer for Scotland.

Simulations using the Met Office Unified Model at 1 km horizontal grid spacing of a Mesoscale Convective System (MCS) with a cold pool which propagated across southern England on 25 August 2005 are validated using detailed observations from the Convective Storm Initiation Project (CSIP). Early organisation of the system is not especially well treated, but the model goes on to form a system which developed qualitative and quantitative features remarkably similar to the observations.

A sensitivity study suggests that the initial linear system is driven by the position of a low-level 'lid' and upper-level instability, the linear organisation being promoted by a weak rear-inflow jet forced by the upper-level warm anomaly in the cloud anvil. A weak cold pool develops in the absence of ice-phase processes, but this does not promote system propagation. Strengthening and descent of the rear-inflow jet, and acceleration of the system, is promoted by the additional heating through glaciation and cooling through snow evaporation. The surface cold pool and gust front are further strengthened by snow melting and rainfall evaporation. With ice-phase processes present, the cold pool strengthens as a result of the system development and its strength is broadly correlated with system propagation speed during the middle phase of the system's lifetime. Propagation enables the convective band to 'sweep up' any convective cells which trigger ahead of the system.

The differing scales of microphysical processes means that it is difficult to form a steady-state system. The observed transition phase corresponds to an increase in the slantwise nature of the flow in the storm and in the low-level cooling by rainfall evaporation near the gust front, combined with a change in ambient conditions (advection over the sea) which eventually enable the cold pool to propagate ahead of the system.

Key Words: convection; precipitation; cold pool; rear-inflow jet; cloud microphysics; mesoscale model

Received 13 September 2012; Revised 25 January 2013; Accepted 21 February 2013; Published online in Wiley Online Library 13 May 2013

Citation: Clark PA, Browning KA, Forbes RM, Morcrette CJ, Blyth AM, Lean HW. 2014. The evolution of an MCS over southern England. Part 2: Model simulations and sensitivity to microphysics. *Q. J. R. Meteorol. Soc.* **140**: 458–479. DOI:10.1002/qj.2142

1. Introduction

This article is a companion to Clark *et al.* (2013), hereafter referred to as Part 1, which describes observations made during the Convective Storm Initiation Project (CSIP; Browning *et al.*, 2007) Intensive Observation Period (IOP) 18, on 25 August 2005 of a Mesoscale Convective System (MCS). As discussed in Part 1, forecasting the occurrence of severe convective storms is of considerable importance for the protection of people and property. Convection-permitting models have become a feasible option for short-range numerical weather prediction; for example, the Met Office's Unified Model (MetUM) now produces operational 36 h forecasts over the UK at 1.5 km horizontal grid spacing. In addition to more routine statistical verification (e.g. Lean *et al.*, 2008), it is important to validate such models against the more detailed observations available from field campaigns. In this article, we compare hindcasts made using the MetUM (at 1 km grid spacing) against the CSIP observations.

Given a reasonably good simulation, the model can be used to gain further insight into the mechanisms operating in the observed system (or, perhaps, in similar systems which might develop in similar circumstances). A considerable body of literature exists on the structure and dynamics of MCSs; this was briefly summarised in Part 1 and excellent overviews are available by Houze (2004) and Cotton *et al.* (2011). The observed system has much in common with the parallel stratiform systems of Parker and Johnson (2000) and Parker (2007b) which develop three-dimensional (3D) structure tending towards trailing stratiform. However, the development of the observed system appears to have some differences. It had a strong cold pool and accompanying low-level jet and gust front, which propagated discontinuously, merging with lines of convection which formed ahead of the system; the first was possibly triggered by gravity waves excited by the system but the second was definitely triggered by sea-breeze convergence possibly modified by orography and evident in fixed boundary-layer convergence some time before cells formed. The system developed a stratiform region which was largely behind the gust front and upright convection, and associated with slantwise ascending motions. Beneath this was a weak downward-slanting rear-inflow jet which, at least later, appeared to help feed the cold pool. This article concentrates largely on these features.

In section 2, we describe the configuration of the model used. Section 3 compares the model with the observed system and shows that, while the early stages of organisation are not well captured, it goes on to develop both qualitatively and quantitatively similar features to those observed. In section 4 we gain further insight into the behaviour of the system by comparing with a reference simulation in which cloud processes are suppressed, thereby establishing the contribution of the system to the mesoscale circulation. In section 5, we perform sensitivity experiments to study the main contributors to formation of the cold pool, rear-inflow jet and the overall system propagation. As will be emphasised below, the objective is to establish the gross role of broad processes such as cooling beneath the anvil, rather than optimise the model simulation. Our conclusions are summarised in section 6.

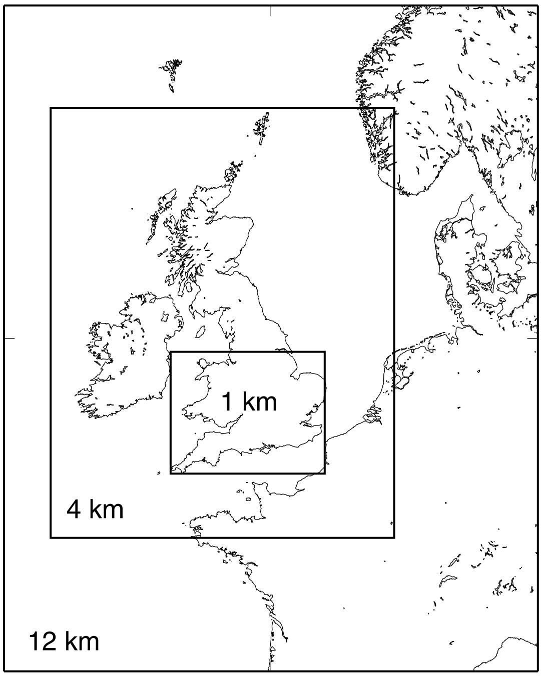

Figure 1. Location of model 12 km, 4 km and 1 km domains.

2. Description of model

The MetUM (version 5 onwards) solves non-hydrostatic, deep-atmosphere dynamics using a semi-implicit, semi-Lagrangian numerical scheme (Cullen *et al.*, 1997; Davies *et al.*, 2005). The model runs on a rotated latitude/longitude horizontal grid with Arakawa C staggering, and a terrain-following hybrid-height vertical coordinate with Charney–Philips staggering. Version 7.6 has been used here. The model includes a comprehensive set of parametrizations, including surface (Essery *et al.*, 2001), boundary layer (Lock *et al.*, 2000), and convection (Gregory and Rowntree, 1990) (with additional downdraught and momentum transport parametrizations), though for the highest resolution runs here the convection scheme was not used. The standard mixed-phase cloud microphysics (Wilson and Ballard, 1999) has been extensively modified to include more prognostic variables. Up to six bulk moisture variables can be used (vapour, cloud water, rain water, ice crystals, snow and graupel), with a single moment (the mixing ratio) describing each. However, various options have been implemented to allow diagnostic treatment of some variables.

Rather than treat the ice crystal and snow hydrometeor categories as two prognostic variables advected separately by the wind field, one simplification is to combine the ice and snow mixing ratios into a single prognostic variable for the advection step and other parametrizations, but to keep the separation within the microphysics parametrization. In this version, the single prognostic ice variable is partitioned into ice crystals and snow aggregates depending on total mixing ratio and temperature, the process rates (formation, loss and conversion to other species, vertical transport) are then calculated as in the full scheme and the two categories are combined again at the end of the microphysics parametrisation step. In practice, for UK convection, it has been found very difficult to show any verifiable benefit from separate prognostic variables for ice crystals and snow and

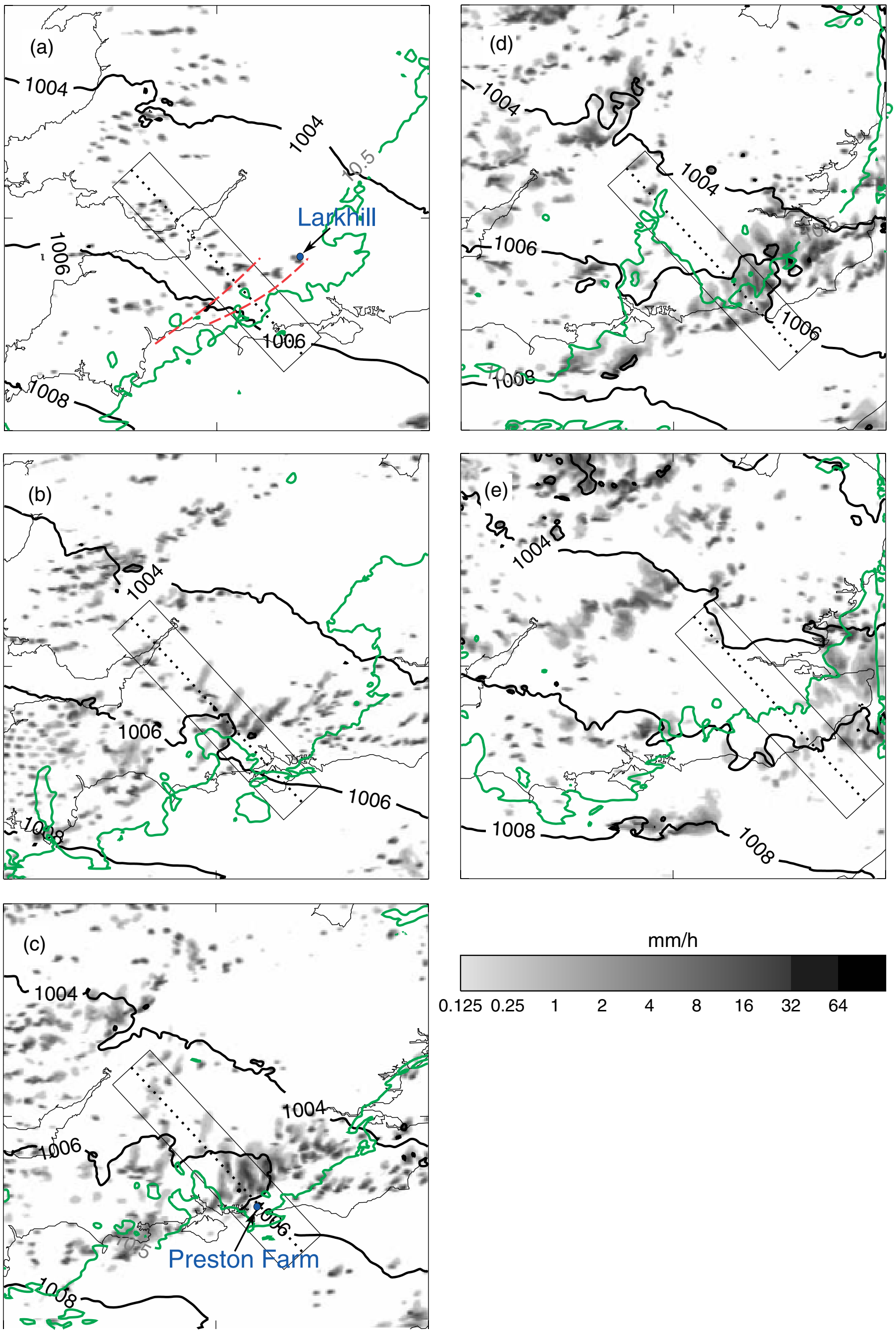

Figure 2. Evolution at hourly intervals from 1000 to 1400 UTC (a)–(e) of 1 km model precipitation (mm h^{-1}, grey shading), mean sea-level pressure (hPa, black contours) and maximum θ_s from 1.8 to 2.4 km above ground (10.5 °C contour in grey, green online) from the reference run. The dotted lines and solid boxes show, respectively, the centre and extent (200 km × 40 km) of average cross-sections shown in subsequent figures. Long dashed lines in (a) show cloud lines tentatively identified by tracking back from 1100 UTC. The location of Larkhill is shown in (a), and of Preston Farm in (c). This figure is available in colour online at wileyonlinelibrary.com/journal/qj

instead, for simplicity, the diagnostic split has been retained for operational forecasting.

Likewise, while no doubt important in some cases, little benefit has been demonstrated using graupel. The systematic impact of prognostic rain is, however, verifiably clear. Prognostic rain has been shown to improve the spatial distribution of rain relative to the mountains in cases of orographic rainfall and also has a systematic impact on lifetime of convective cells, presumably through interaction with cell downdraughts (R. M. Forbes, unpublished). In this case, a run with the full six-phase microphysics has been performed; it will be shown later that it differs in only minor detail from a run with a single ice phase, because little or no graupel is formed and the diagnostic split between ice crystals and snow does a reasonably good job of reproducing the behaviour of the full scheme.

Subsequent sections will describe sensitivity studies involving changes to the microphysics. The choice of parameters used in the single-moment scheme is a compromise which has been found adequate for operational forecasting of both stratiform and convective precipitation over the UK. It is likely that a higher-order scheme would have a significant impact on the development of an MCS, as both convective and stratiform regions are important and are likely to have markedly different microphysical properties. However, the objective is not to optimise the model; it may

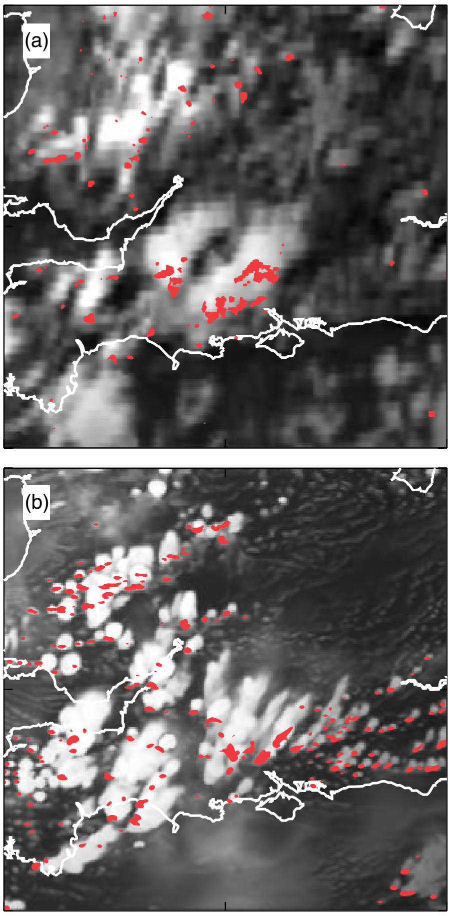

Figure 3. Comparison at 1100 UTC of (a) the observed MSG infrared image (greyscale) and network radar rainfall rate (areas over 4 mm h^{-1} in dark shading, red online) with (b) 1 km model broadband long-wave radiance temperature and rainfall rate. This figure is available in colour online at wileyonlinelibrary.com/journal/qj

be the case that better simulations could be achieved using more sophisticated microphysics or different parameter values. Instead, we are deliberately restricting ourselves to looking at the gross impacts of microphysics, primarily the additional latent heating and cooling from including frozen species, and the slower fallout compared with rain. It is likely that significant, but hopefully more subtle, impacts would be found by considering other microphysics schemes (e.g. dual-moment schemes which allow the number density to vary independently of the mixing ratio). Changes to rates of microphysical processes can, of course, have widespread consequences; – for example, the direct impact of cloud condensation nuclei concentration on cloud-drop size and hence warm rain production is well known, and more recent work has shown consequential impacts on ice concentrations and evolution (e.g. van den Heever *et al.*, 2006). The more detailed assessment of the impact of additional microphysical variables (including higher-order schemes) will be the subject of future work.

Care must be taken in comparing microphysics schemes – for example, the added degrees of freedom provided by additional moments to describe size spectra may primarily mean that average properties differ from those predicted by a single-moment scheme, an effect that could be reproduced by changing the average properties of the single-moment scheme. Furthermore, an ensemble approach is required to demonstrate the true impact of changes at this level, as individual realisations can show misleadingly high sensitivity to model changes, since cloud evolution can be highly sensitive to even very small perturbations (Leoncini *et al.*, 2013; Morrison, 2012). However, in arriving at these simulations, we have used a number of variations in model configuration to be confident that the overall behaviour and sensitivities discussed below are at least qualitatively robust. For example, earlier studies used a configuration with horizontal grid spacing 1.5 km rather than 1 km; there were, of course, quantitative differences from the results presented below, but these were small and did not change the broad conclusions reached.

Operationally, at the time of CSIP, the Met Office ran a ‘mesoscale’ domain operationally with horizontal grid spacing 0.11° (∼12 km) and 146 × 182 points in the horizontal. This was one-way nested inside a global version with horizontal grid spacing 0.83 × 0.56° (approx. 60 km at midlatitudes). Both models ran with the same 38 levels spaced non-uniformly in the vertical. The 12 km model has its own 3D-Var data assimilation scheme; to maintain balance the analysis increments are nudged in over a 2 h window centred on the nominal analysis time. The MetUM has been run at higher resolution, one-way nested at 0.036° (∼4 km) and 0.009° (∼1 km) horizontal grid spacing using the 12 km model state at 0700 UTC from the 0600 UTC 25 August 2005 operational 12 km analysis as initial conditions, i.e. at the end of the analysis nudging period. The 4 km domain was that adopted for operational UK forecasting after CSIP and so covers the whole UK with 288 × 360 points. It used lateral boundary conditions from the same 12 km forecast (so our results represent a genuine hindcast).

The 1 km domain (516 × 408 points) was chosen as a general domain for the CSIP area, extended north to avoid having the Welsh mountains on the northern boundary, and has been tested against UK convection cases for a number of years (Lean *et al.*, 2008). The domains are shown in Figure 1. The 12 km and 4 km models were run with 38 vertical levels and the 1 km model with 76 (alternate levels coinciding with the 38-level set). This level spacing is stretched away from the surface, so there are 13 wind levels below 1 km and 20 below 2 km. The 1 km model is run with no convection scheme and enhanced microphysics (see below). Only the 1 km results are considered here. The 1 km domain is large enough to cover the MCS life history over the UK from initiation to crossing the English Channel.

3. Validation of model representation of the evolving MCS

A horizontal grid length of 1 km is insufficient to represent, in any detail, individual convective cells, but it has been found that mesoscale organisation of cells is often reproduced well and, in this case, we are primarily interested in the cold pool and rear-inflow jet development. This is consistent with the findings of Weisman *et al.* (1997) and Bryan *et al.* (2003), though the systems they studied were somewhat deeper and more energetic. Though the 1 km model initialized from lower-resolution data can, in general, suffer from spin-up (Lean *et al.*, 2008), this is less of an issue in this case since we are starting the run before the initiation of the cells which develop into the MCS.

The observed MCS developed from an initial line of showers (identified as Line B in Part 1) between about 0730 and 0930 UTC. This underwent a complex transition

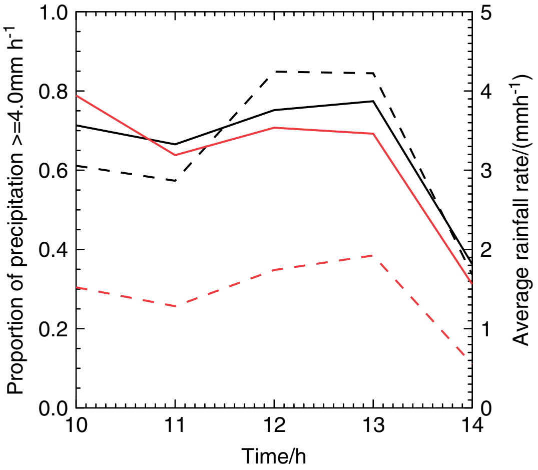

Figure 4. Analysis of network radar rainfall rates (composite of 1, 2 and 5 km products, black) compared with the model (grey, red online) at hourly intervals 1000 to 1400 UTC on 25 August 2005 identified as part of the MCS. Solid line (left-hand scale) gives the proportion of the total rainfall provided by rates over $4\,\mathrm{mm\,h^{-1}}$. Dashed line (right-hand scale) shows the average rainfall rate where above $0.05\,\mathrm{mm\,h^{-1}}$. This figure is available in colour online at wileyonlinelibrary.com/journal/qj

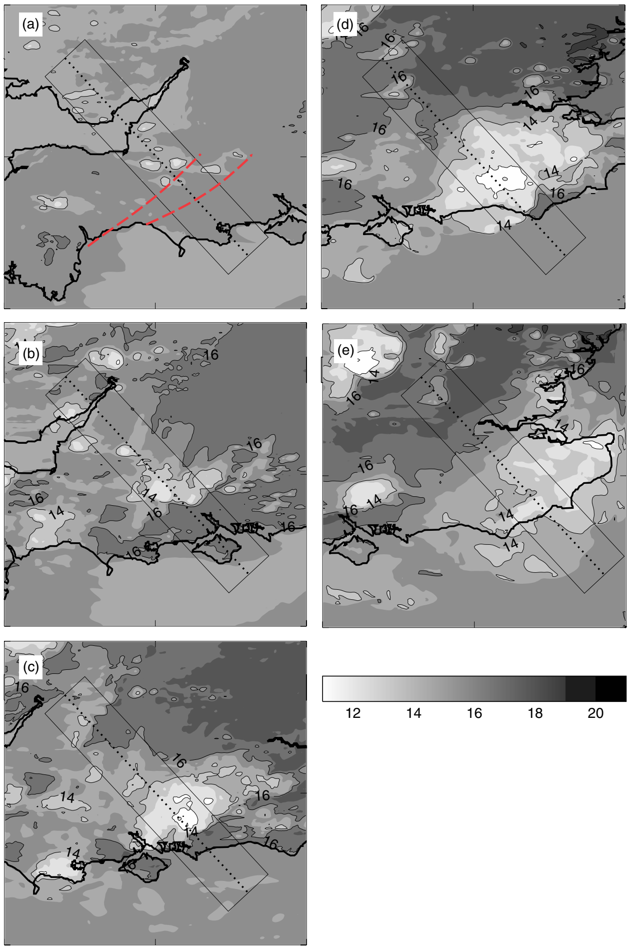

Figure 5. Evolution of 1 km model forecasts at hourly intervals from 1000 to 1400 UTC (a)–(e) of lowest model level (5 m) potential temperature (°C). The dotted lines and solid boxes are as Figure 2, and long dashed lines in (a) show cloud lines tentatively identified by tracking back from 1100 UTC. This figure is available in colour online at wileyonlinelibrary.com/journal/qj

between about 1030 and 1130 UTC in which lines of new cells forming ahead of this line merged with the system (Lines C and D), some likely to have been independently triggered by a sea-breeze convergence line (Line D), generating a strong surface cold pool and gust front. Eventually (after 1230 UTC) this propagated over the sea as an arc cloud and bow echo (Line E).

Figure 2 shows the overall evolution of precipitation in the model. The initial line of convective cells does not form in the model, but a deep, intense cell does form very close to the cell which intensified in the northern half of Line B close to the coast in the Severn Estuary at about 0900 UTC. By 1000 UTC, other intense cells have developed in the vicinity, along with an area of scattered, weaker cells to the east (Figure 2(a)).

There is little evidence of linear structures in the rainfall distribution. However, examination of cloud shows clear linear structures by 1100 UTC; Figure 3 shows a comparison of observed cloud – the Meteosat Second Generation (MSG) infrared (IR) image – and associated precipitation with an indication of deep cloud derived from the model radiation scheme total outgoing long-wave radiation, expressed as a radiance temperature using Stefan's Law assuming emissivity of 1. This is not strictly the same as a narrow-band IR satellite image, but gives similar qualitative information about high cloud.

The comparison shows that by 1100 UTC clear lines had developed in the cloud, with some minor cells ahead. Backtracking to 1000 UTC one may tentatively identify two lines, marked by long dashed lines in Figure 2(a). These resemble, in position and orientation, observed Lines B and C (Part 1). Note, however, that (much as in the early stages of Line C) the cells ahead of the line identified in Figure 2(b) are less clearly formed in a line. The southern part of the observed developing MCS corresponds well with the most intense cluster of cells at the head of a distinct positive surface pressure anomaly in the model, but it is clearly not as organised in the model at this stage. Furthermore, the rainfall distribution is marred by the presence of smaller and less intense cells which triggered over southeast England ahead of the system. Similar clouds are clearly visible in the MSG IR image. These areas appear to be associated with orography (typically ∼100 m and peaking at ∼200 m above sea level). As discussed in Part 1, similar cells did trigger along the south coast about half an hour later, but those further inland are not evident in observations until about an hour later.

By 1200 UTC (Figure 2(c)), a very distinct leading edge of intense cells exists, coincident with the leading edge of the (now more extensive) positive pressure anomaly. Behind this is a region of moderate precipitation. This region is close to and resembles the observed system at this time (Part 1, Figure 14(g)), though it extends further northeast and is somewhat less 'bowed'. This system goes on to overtake cells developing to the east, similarly to the observed system, and eventually the leading edge accelerates forward of the main cluster, crossing the English Channel and producing a distinct cloud arc with much weakened rain as it does so (Figure 2(e)). (More detailed comparisons with observations are shown below.)

Figure 4 compares the mean rainrate and fraction over $4\,\mathrm{mm\,h^{-1}}$ (a surrogate for the convective fraction) from the model with the observations. The convective fractions are remarkably similar, though there is less evidence of intensification between 1100 and 1200 UTC; however, the overall mean rate is about half in the model than

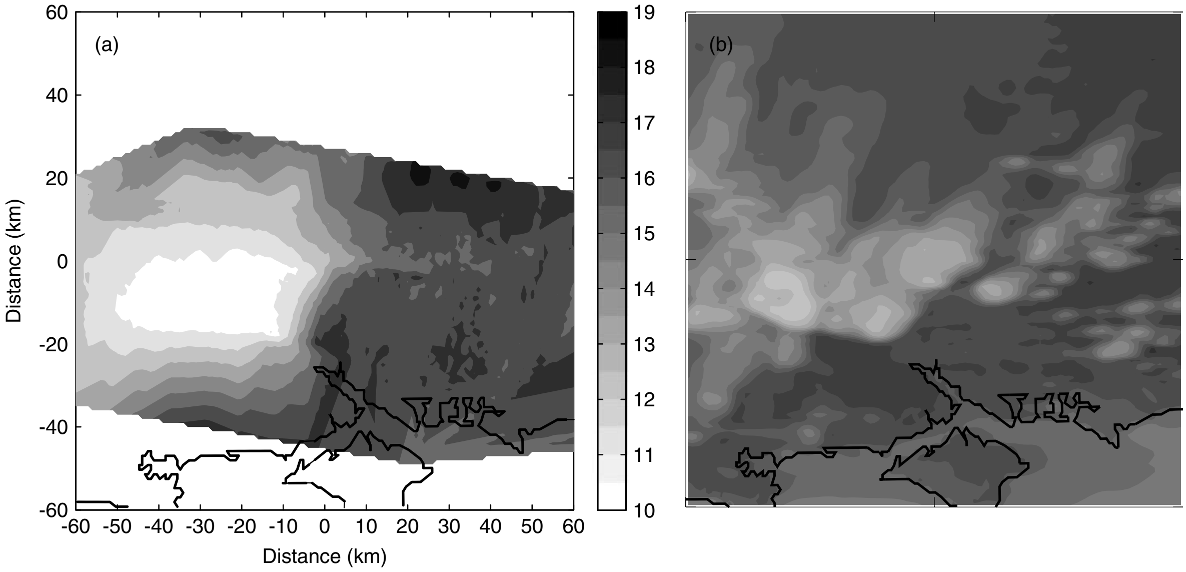

Figure 6. Comparison of potential temperature (°C) at 1100 UTC from (a) analysis of surface observations and (b) model lowest level.

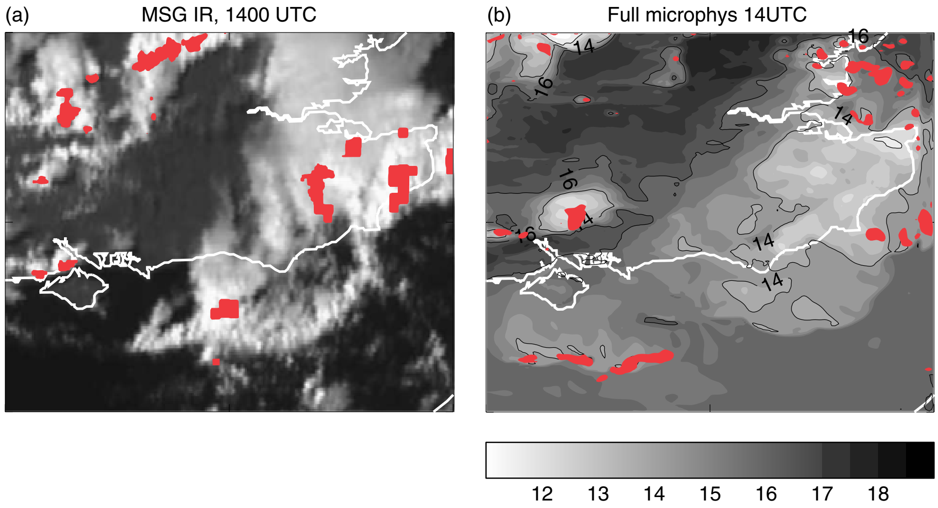

Figure 7. Comparison at 1400 UTC of (a) visible MSG image (shading) and radar rainfall rate over 4 mm h^{-1} (dark areas, red online) with (b) modelled bottom-level potential temperature (contours with shading) and rainfall rate over 4 mm h^{-1} (dark areas, red online. This figure is available in colour online at wileyonlinelibrary.com/journal/qj

in observations, suggesting that the system as a whole is somewhat less intense. Note that these data are taken over subjectively determined limits to the MCS.

As suggested by the positive pressure anomaly (Figure 2), the line of intense convective cells develops at the edge of a surface cold pool which grows in area and intensity with time. Figure 5 shows the model forecast of potential temperature at the lowest model level. The early stage of development of the cold pool is evident at 1000 UTC (Figure 5(a)) as a set of distinct regions associated with the cells discussed above. By 1100 UTC (Figure 5(b)) these have merged into one contiguous region, though there remains some suggestion of two separate pools – one associated with the cloud line ('B') and one associated with the convection ahead of it at its northeast end. By 1200 UTC (Figure 5(c)) the model shows a sharp surface front at the southeast edge of the cold pool with a minimum temperature some distance behind. The forecast lowest near-surface potential temperature in the cold pool is about 12 °C. By 1300 UTC the cold pool is larger and the lowest temperature remains about 12 °C, a drop of up to about 5 °C from surrounding air over land. Figure 5(d) and (e) shows the cold pool propagating over the English Channel and warming as it does so (as sea-surface temperatures are higher than those of the cold pool). (Another, weaker, cold pool is evident to the west in Figure 5 which does not correspond closely to any observed.) Over land the eastern end of the model MCS is merging with cells which triggered and intensified to the east (analogous to Line F in the observations).

The surface cold pool at 1100 UTC can be compared with the analysis of surface observations in Part 1; this comparison is shown in Figure 6. The comparison confirms that the model cold pool is similarly located but less intense (by about 2 °C), and also less distinct because of the cold downdraughts from the precipitating cells to the east. However, the observational analysis was based on making a quasi-steady-state assumption, displacing surface temperatures according to an assumed propagation speed, and most of the lower temperatures were observed after 1100 UTC, so there may be a bias in Figure 6(a). One site did observe temperatures lower than 12 °C before 1100 UTC, so the model does appear to be too warm. By 1200 UTC (Figure 5(c)) the modelled cold pool is more extensive than observed at 1100 UTC and more distinct from the cells to the east, so it would appear that the temporal development is similar but somewhat delayed (by perhaps half an hour or so), with a slight warm bias.

The presence of the cold pool later in the MCS development was evident in visible MSG imagery in the form of a rope cloud propagating across the English Channel ahead of the main precipitation area. Figure 7 shows this alongside the model 5 m potential temperature and rainfall. The correspondence between the two is remarkably good for the main cold pool, though, as already noted, a second smaller and weaker pool exists to the southwest in the model, somewhat further advanced than the position suggested by the satellite imagery.

Vertical profiles just before deep convection triggered (1000 UTC) are shown in Figure 8. The model profile is taken approximately 10 km southeast of Larkhill as, by chance, a convective cell triggered close to Larkhill at this time (Figure 2), as incidentally happened in the observations about 10 min later. The model profile is extremely comparable to the observations. There are some small differences: the tropopause is less distinct and a little colder in the model, and the upper-tropospheric dry region starts higher in the model, reflecting a slightly slower encroachment of the upper-level low θ_s air. (θ_s is the wet-bulb-potential temperature (θ_w) the air would have if saturated (Ludlam, 1980); if a parcel of air with given θ_w is lifted moist adiabatically to a level with given θ_s, then if $\theta_w > \theta_s$ the parcel is positively buoyant.) An intermediate lid exists at around 500 hPa in both profiles, though it is also perhaps 50 hPa lower in the observations. Below this, both profiles are similarly moist, though the model is a little moister below 850 hPa. Finally, the model is slightly cooler (about a degree C) at the surface, though the overall boundary-layer potential temperature is very similar.

Figure 9 shows wind hodographs corresponding to these vertical profiles; the model is extremely comparable with the observed profile, but a little backed and weaker. However, an average taken ahead of the system (from 160 to 180 km along the cross-sections at 1000 UTC, shown later) is much closer to the observations. All the profiles show a strong shear in wind speed consistent with the horizontal temperature gradient, together with moderate directional shear, backing about 40° from 900 to 400 hPa. The initial line (equivalent to the observed Line B) is approximately aligned with the shear vector (so the cross-sections shown later are approximately perpendicular to it). In the context of 2D squall lines, this profile resembles the constant shear case of Thorpe *et al.* (1982), which does not lead to a long-lived system. The low-level shear is relevant in that it is necessary to oppose the propagation of the cold pool relative to the storm; indeed, as discussed above, it is likely that it is the combination of strengthening cold pool and reduced low-level shear over the sea which results in the cold pool eventually running ahead of the system. However, the directional shear present means that it is likely to be more helpful to discuss the structure in terms of the discussion by Parker (2007b). In fact, the wind profile has much in common with the control simulation of Parker (2007a). As discussed in Part 1, the system evolves broadly in the same way as the parallel stratiform systems studied by Parker (2007b), in particular, the initial linear system evolves into a distinctly 3D system, dominated by (backbuilding) convection at the upshear end and with an increasing component of stratiform precipitation downshear, gradually developing trailing stratiform characteristics.

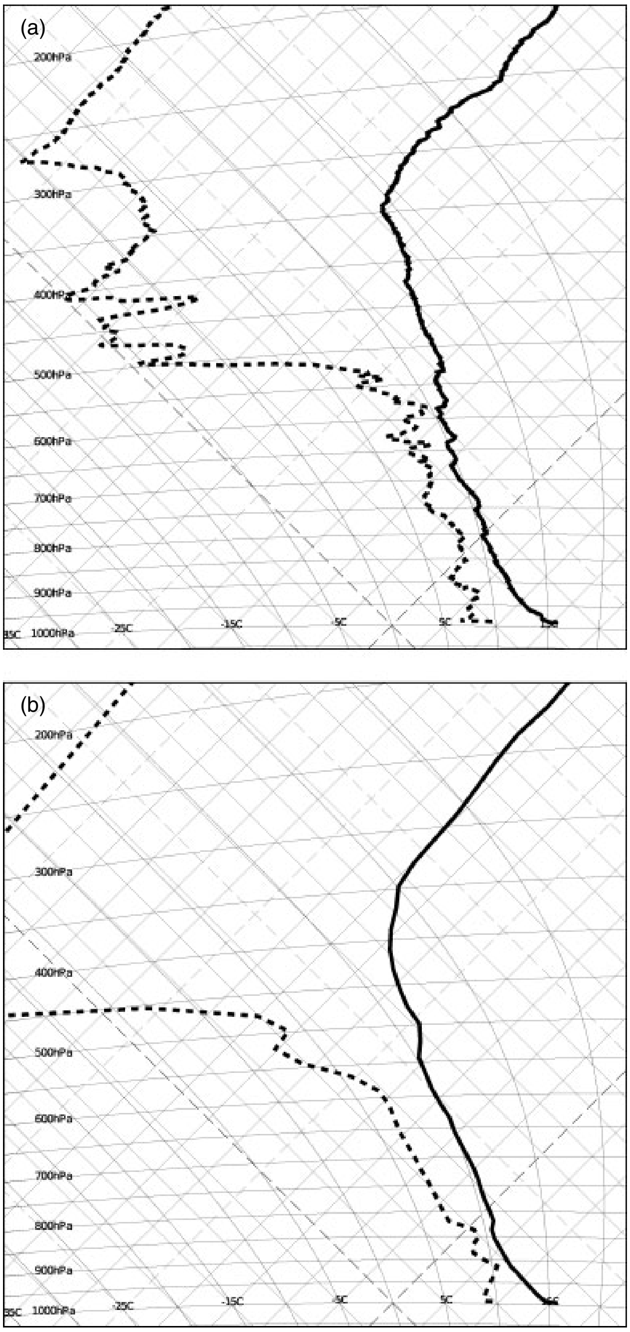

Figure 8. Tephigrams nominally at 1000 UTC showing (a) observed and (b) modelled profiles of temperature (solid) and dewpoint (dashed) (a) at Larkhill and (b) approximately 10 km southeast of Larkhill (51°12′N, 1°48′W). Figure 2(a) shows the location.

The time variation of the vertical thermodynamic structure in the model is compared with radiosonde data in Figure 10. This shows the approach of upper-level low-θ_s air associated with the upper-level potential vorticity (PV) anomaly and lowered tropopause. This is separated from the near-surface air by a higher θ_s ‘lid’ between 900 and 850 hPa. The arrival of the surface cold pool and associated convection is evident in the model cross-section at 1200 UTC. This coincides with the erosion of the lid. It is evident that

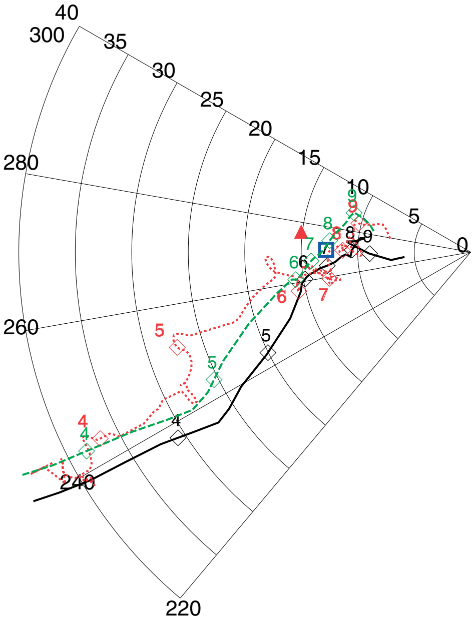

Figure 9. Hodographs nominally at 1000 UTC of observed (dotted, red online) and modelled (solid black) wind corresponding to profiles in Figure 8. In addition the average wind from 160 to 180 km along the cross-sections in Figure 14(a) is shown (dashed, green online). Pressure levels are marked with a numbered diamond every 100 hPa, labelled in hPa/100. The observed estimated cell velocity is labelled with an open square, and the observed cold-pool propagation velocity with a filled triangle. This figure is available in colour online at wileyonlinelibrary.com/journal/qj

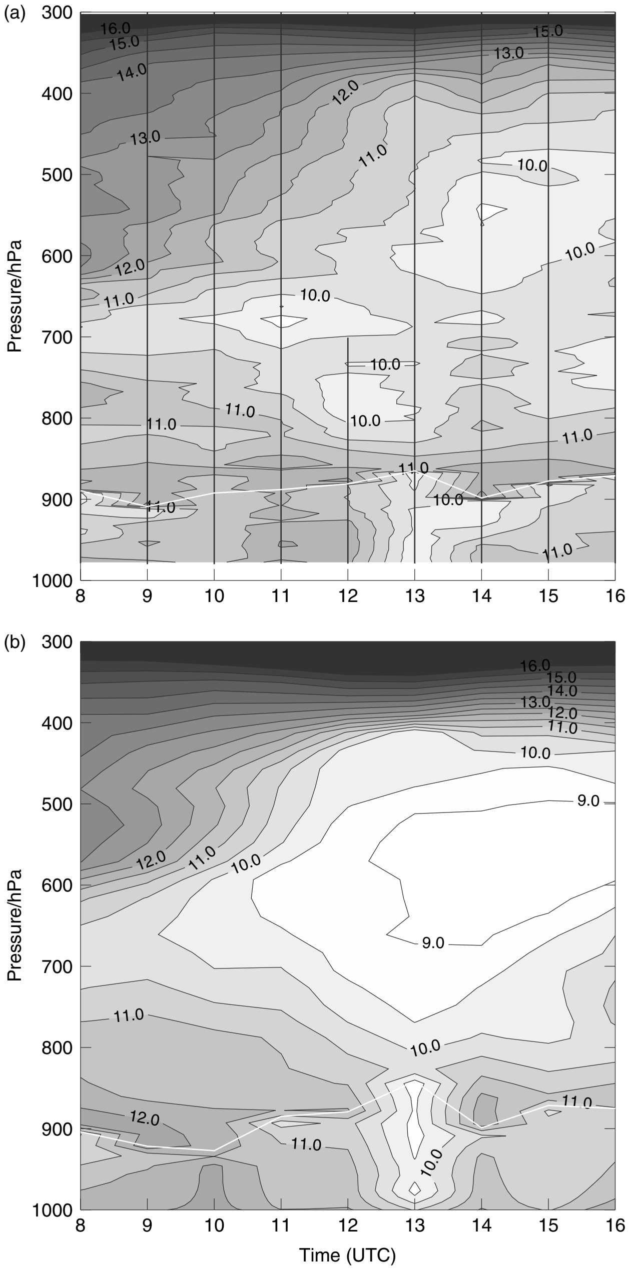

Figure 10. Time–height cross-section at Preston Farm constructed (a) from hourly radiosonde observations and (b) from the model (10 min averages every hour). The solid white line indicates the lifting condensation level (LCL) assuming a parcel derived from the 1000–950 hPa layer. The contours (°C) are of θ_w beneath the LCL and θ_s above.

there were near-triggerings earlier in the model, but this is less evident in the observations. This may simply reflect the sparsity of the hourly observations, but may also be consistent with the tendency to trigger sooner in the model further east. Radar rainfall and surface observations at other sites suggest that the surface cold pool arrived very shortly after 1200 UTC; this is not evident in the cross-section as the 1200 UTC ascent was slightly ahead of the cold pool, but the short life of the radiosonde was probably due to it being struck by lightning, which was noted by observers at the time.

The ascents associated with the cold pool are shown in detail in Figure 11. Since the leading edge reaches the location of the Preston Farm sonde site (Part 1) just before 1200 UTC, a matter of a few minutes before that observed, we have chosen a point a little further east (17 km) for comparison. The overall structure is very similar, with a region of greater cooling from the surface to about 975 hPa, and a region of more moderate cooling above up to about 875 hPa. The ‘pre-cold-pool’ boundary layer is less than 0.5 °C colder than observed and the degree and depth of cooling is significantly less than observed. Humidity changes are not dissimilar in the cooling region, but the model shows a distinctly drier layer above 800 hPa. It must be emphasised that the cold pool is fairly inhomogeneous – choice of different locations yields significantly different (though qualitatively very similar) results. Nevertheless, the comparison gives some confidence in the model results, though consistent with the idea that the system develops a little less quickly or less intensely than observed.

The Chilbolton RHI cross-sections shown in Part 1 showed the presence of a low-level jet behind the gust front, with some evidence of this being at the head of a more or less contiguous downward-sloping forward flow originiating from mid levels – this may be identified as a weak rear-inflow jet. Figure 12 shows a comparison between the observed Doppler velocity from RHIs close to 1230 UTC and cross-sections in the model. The cross-sections are centred along the same directions as the observations, but displaced 10 km away from Chilbolton, and averaged over ±5 km either side of the line in order to smooth out some of the variability. It must be emphasised that the system shows substantial variability along the gust front, and there is little possibility of matching the detail in the observations. Nevertheless, the model has a great deal in common with the observations. All show the low-level jet with similar strength to the observations, together with rearward sloping upper-level flows, and a suggestion of the steeply ascending flow associated with the cell updraughts. The rear-inflow

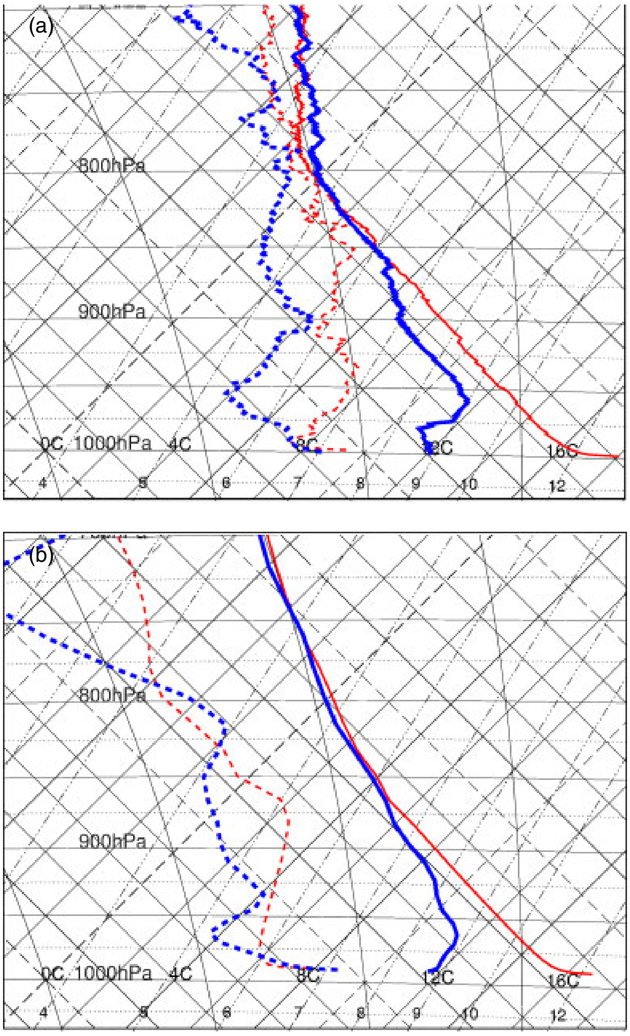

Figure 11. Tephigrams showing (a) radiosonde and (b) model profiles of temperature (solid) and dewpoint (dashed) at a point about 10 km east and 10 km south of Preston Farm (50°53′N, 0°47′W); Figure 2(c) shows the location. Thin lines are ahead of the gust front (1200 UTC), and bold ones behind (1300 UTC). This figure is available in colour online at wileyonlinelibrary.com/journal/qj

jet is evident, becoming stronger to the downshear end of the system. In the cross-sections shown, the modelled rear-inflow jet appears somewhat stronger than observed, though this may be an artefact of the cross-sections chosen. No direct comparison with reflectivity has been made (since it would rely on our choice of model relating hydrometeor mixing ratio to reflectivity), but contours of significant concentrations of ice and rain are shown on the model cross-sections; these may be roughly compared with the envelope of Doppler data since these data are only available where sufficient reflectivity exists. Broadly the same trend is shown as one moves from the southernmost cross-sections (Figure 12(c, f)) to the northeast. To the south the system is quite upright, with much weaker low-level jet and little reflectivity behind the gust front. To the northeast, the slantwise motions are much clearer and stronger, with substantial ice in the rearward sloping updraught behind the gust front, but also a suggestion of somewhat forward-leaning anvils at the leading edge. (Note that this reflects the structure at the mature stage of the parallel stratiform systems of Parker (2007b), with a transition to a more trailing stratiform structure as one moves downshear.) This comparison certainly highlights the limitations of the relatively poor model resolution at cell scale; variability is at a larger scale and probably a larger amplitude. Given the variability of the system, it is impossible to make a direct comparison with the radar observations, but the similarity at this stage is extremely encouraging.

In summary, the early linear phase of the observed system discussed in Part 1 is, at best, only hinted at by the model simulation, but this has little impact on its subsequent organisation, perhaps delaying it somewhat but not radically changing the eventual evolution. Thereafter qualitative features of the system are very similar to the observations. The position and propagation speed of the system is well reproduced; in fact the system velocity is, at least at the early stages, dominated by ambient mid-level advection, not only of the convective cells, but the rearward edge of a weak, inhibiting 'lid'. As a result, surface cold pools rapidly coalesce so that, by 1200 UTC, the leading edge of the cold pool is propagating with the system. The model compares well with the only radiosonde ascent that penetrated the cold pool, though this ascent was 50 km behind the leading edge and the model shows substantial variability. The model cold pool may be a little too weak and shallow, but its variability makes it difficult to be certain.

Model cross-sections have very much in common with the Chilbolton radar data. The absence of observed reflectivity above 5 km (and the MSG cloud-top height) suggests that there may be somewhat too much ice at high levels in the model, though we have not computed model reflectivity or accurate IR radiance (since such estimates would depend a great deal on assumptions regarding particle size anyway). The rear-inflow jet appears to be reproduced, as far as the radar data enable a comparison to be made; there is some suggestion it may be stronger in the model. The strengthening of the jet at low levels close to the front is also well reproduced, though the jet is perhaps somewhat deeper in the model (contrary to the depth of the cold pool suggested by the sonde ascent).

The later development, in which the cold pool ran ahead of the main cloud and precipitation, accelerating as is crossed the English Channel but failing to trigger new cells, seems exceptionally well captured by the model.

4. Contribution of the developing MCS to the mesoscale circulation

It is of interest to evaluate more precisely the contribution of the MCS development to the overall flow. In idealised studies, one generally has a reference or upstream profile with which to compare. In real cases such as this, the underlying state is varying in space and time, and it is not even straightforward to define precisely what is meant by a reference state. Area-average profiles (perhaps taken from a lower-resolution model) are an option but clearly include the average impact of the convection. We have created a time- and space-varying reference by running the model with the diabatic impact of cloud microphysical processes, including cloud condensation, turned off. The latter was achieved by setting the latent heats of condensation and freezing to a negligible value ($1\,\mathrm{J\,kg^{-1}}$). The radiative heating and cooling of cloud was also turned off. It must be recognised that, in so doing, the boundary-layer behaviour is changed. The direct impact, changing the sensible and latent heat fluxes, may not be so important as θ_w should not be markedly

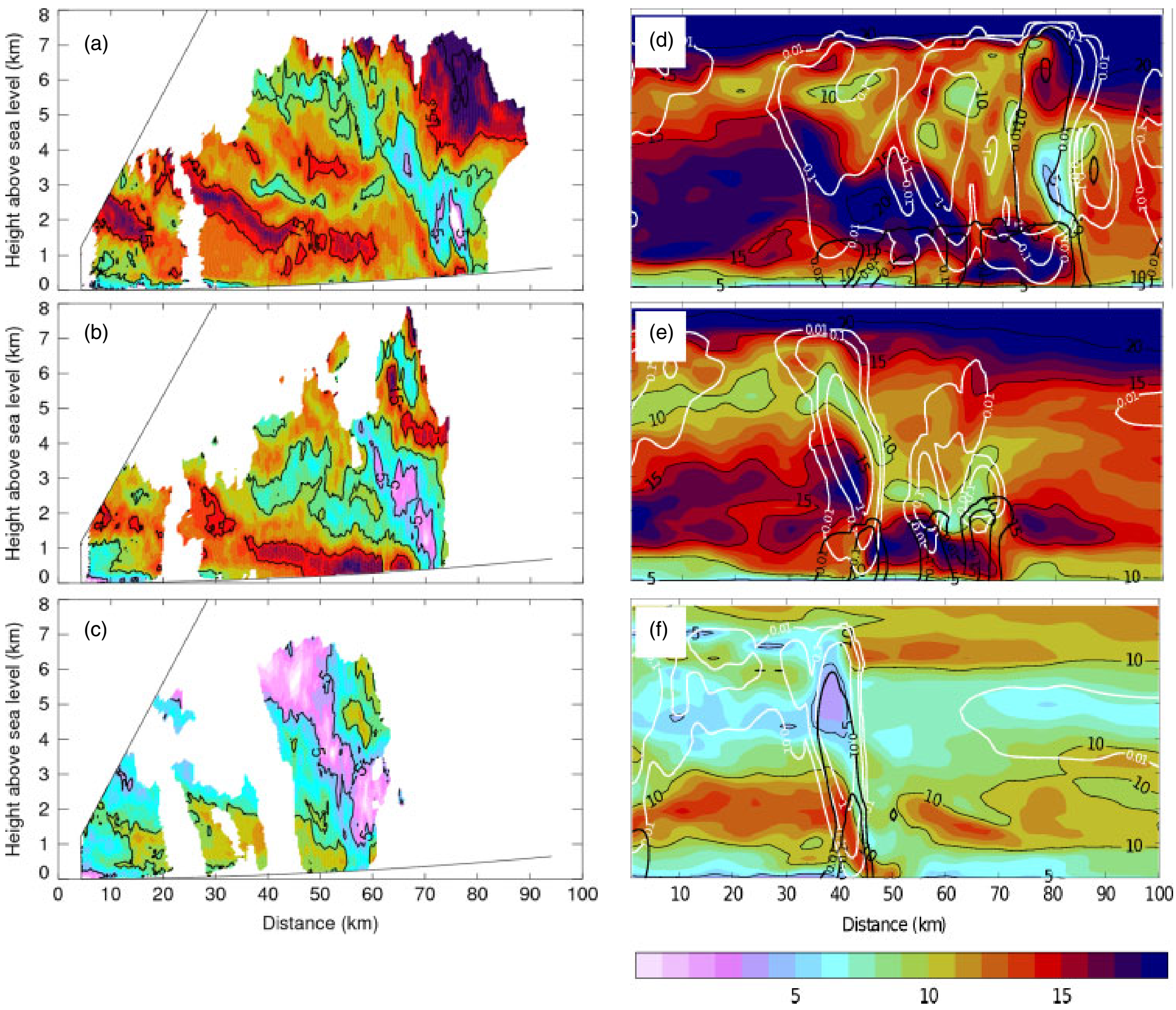

Figure 12. RHI scans of Doppler radial velocity from Chilbolton CAMRA radar at (a) 1229 UTC, 100° azimuth, (b) 1228 UTC, 120° azimuth, and (c) 1226 UTC, 143° azimuth. (d)–(f) show equivalent cross-sections starting from Chilbolton along the same directions, averaged over a 10 km wide strip, showing the along-section wind speed in the model plus contours of ice (white) and rain (bold black). This figure is available in colour online at wileyonlinelibrary.com/journal/qj

changed, but the incoming short-wave radiation will be smaller where there is cloud in the full model. However, this is very difficult to avoid and, so long as this is recognised, this configuration forms a valuable reference, especially as the impact of cumulus cloud on incoming short-wave radiation is relatively small.

To establish the MCS contribution to the flow, we have concentrated on a number of cross-sections. Each is oriented in the direction of the strongest propagation direction of the gust front, but they move east approximately with the system. The locations of these cross-sections are shown in Figures 2 and 5. There is some spatial variability along the squall line (as distinct cells exist along the line), so individual cross-sections such as those in Figure 12 may be a little misleading. To overcome this, we have averaged over a 40 km wide swath along lines approximately aligned with the gust front. Data have been interpolated to 1 km intervals, then averaged. Though individual cross-sections generally show broadly the same features, it must be remembered that any inferred flows represent the dominant flow averaged across the MCS, and some localised flows in the reverse direction may exist. Note also that these cross-sections are more than twice as long as the observed cross-sections shown in Figure 12. It will be shown that these cross-sections summarise the impact of the system well; however, it must be emphasised that they are located approximately perpendicular to the strong wind shear, and so should not be regarded as cross-sections of a 2D system.

Figure 13 shows the reference cross-sections. They are only shown every 2 h as the development in between is very slow. The wind and cloud plots (Figures 13(a)–(c)) are relatively uniform, reflecting the fact that much of the shear is perpendicular to the cross-section. There is some development in time, however; most notably at 1000 UTC there is a horizontal region of higher wind speed between 2 and 3 km up to 150 km along the cross-section, beneath a horizontal region of lower wind speed above 6 km. By 1400 UTC this has developed into a region of relatively stronger wind (up to 11 m s^{-1}) slanting from about 5 km at the northwest end to between 1 and 2 km at the southeast end. This (fairly weak) structure may be an inertia-gravity wave, and one cannot rule out the possibility that it is an artefact of the slight imbalance with the lateral boundary conditions induced by turning off the cloud processes.

The cloud fraction contours show regions near to saturation; a low-level layer corresponds with the lifting condensation level shown in Figures 13(d)–(f)); in the full model, convective cloud (possibly shallow – see below)

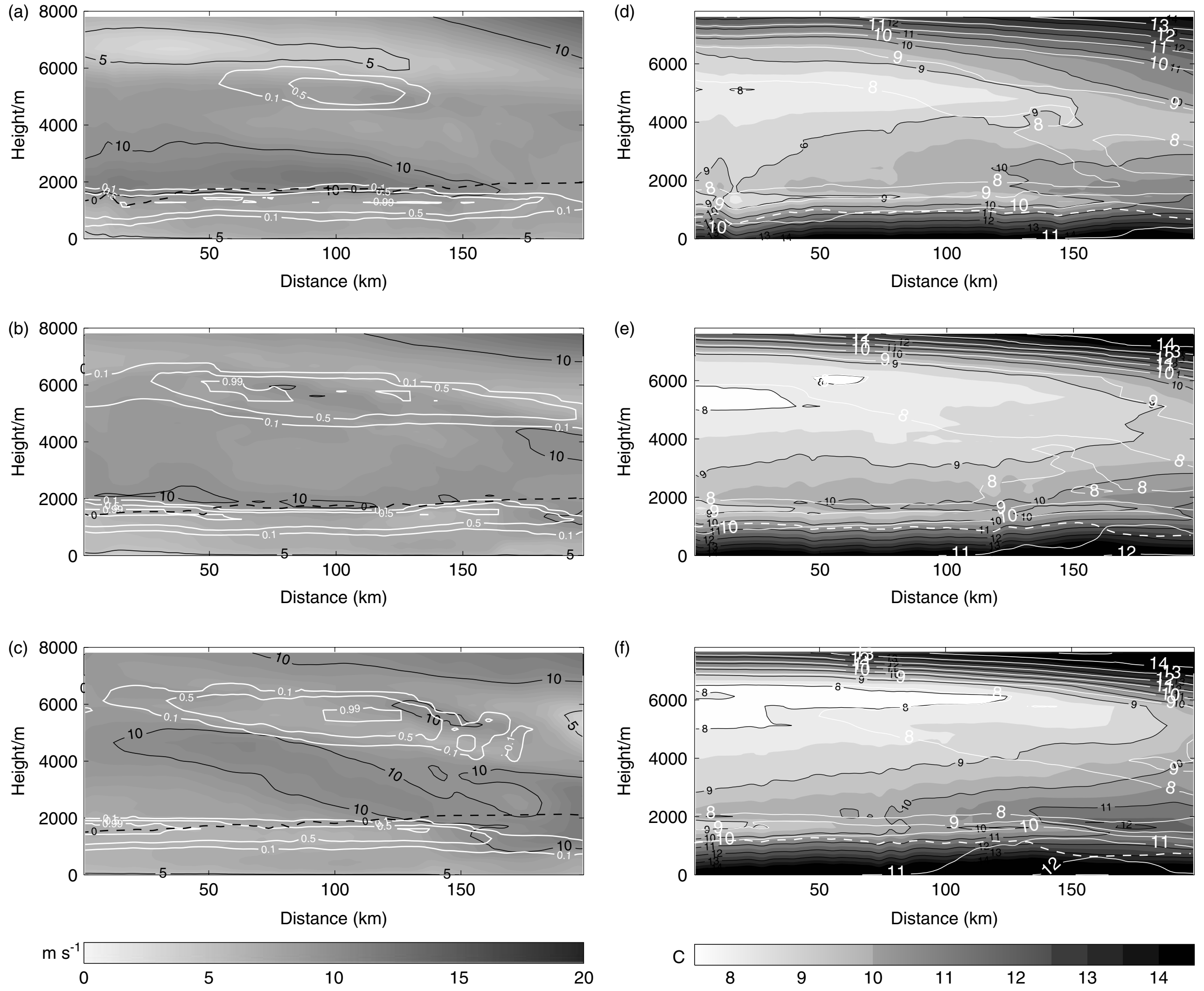

Figure 13. Vertical cross-sections from model forecasts from the 1 km horizontal grid reference model at (a, d) 1000 UTC, (b, e) 1200 UTC, and (c, f) 1400 UTC. (a, b, c) show horizontal wind speed along the direction of the cross-section (shaded thin black contours at 5 m s^{-1} intervals), the cloud fraction (bold white contours), and the freezing level (dashed black line). (d, e, f) show θ_s (shaded black contours at 1 °C intervals), θ_w (solid white contours), and the lifting condensation level from surface (dashed white line). Cross-sections are averaged (at 1 km intervals) over the regions shown in Figures 2 and 5.

would form here and, of course, release latent heat, so we expect the reference model to be significantly cooler than the full model in this region. A second layer of cloud forms at upper levels, sloping from 6 km at the northwest end to 5 km at the southeast end. This is a distinct region behind the frontal passage, presumably reflecting large-scale ascent ahead of the upper-level PV anomaly. This corresponds well with the unstable region and reflects the mechanism of destabilisation.

The θ_s plots (Figures 13(d)–(f)) broadly reflect the structure shown in Figure 10, with an upper-level region of low θ_s (8 °C or below) to the northwest behind a region with upward-sloping θ_s contours. Beneath this, θ_w is between 10 and 11 °C below the lifting condensation level, reflecting conditional instability. The region between 100 and 150 km along the cross-section is a clear transition region. It marks the leading edge of the upper-level low-θ_s region to the northwest, the trailing edge of a low-level higher-θ_s 'lid' (10 °C or above) at about 2 km to the southeast and a region of lower θ_w above the 'lid' between 2 and 3 km. Consistent with the relative flow, the lid moves slowly left (northwest) relative to the cross-section but this is accompanied by an increase in low-level θ_w at the leading edge of the system to above 11 °C, so the effective lid remains fairly stationary with respect to the cross-section. Note that this lid is less clear in the full run at later times; the θ_s structure (not shown) ahead of the system is similar, but within the system the convection serves to homogenize θ_s in the layer.

To give some idea of the location of this lid, contours from the reference run of the maximum θ_s between 1.8 and 2.4 km above the surface have been plotted on the full model precipitation plots in Figure 2. Only the 10.5 °C contour is shown to indicate the approximate position of the edge of the lid in the reference run. At 1000 UTC, while there is clearly a certain amount of spatial variability, the leading edge of convection clearly corresponds very well with this boundary. Later, some convection initiates on the warm side of it, but only over the elevated ground of the North and South Downs in southeast England and/or close to the coast as noted above. This reflects the weakness of the lid; convection initiates a little earlier to the northwest of it, but only very small perturbations are required to initiate triggering under it. However, this contour continues to mark the leading edge of convection quite well until 1300 UTC,

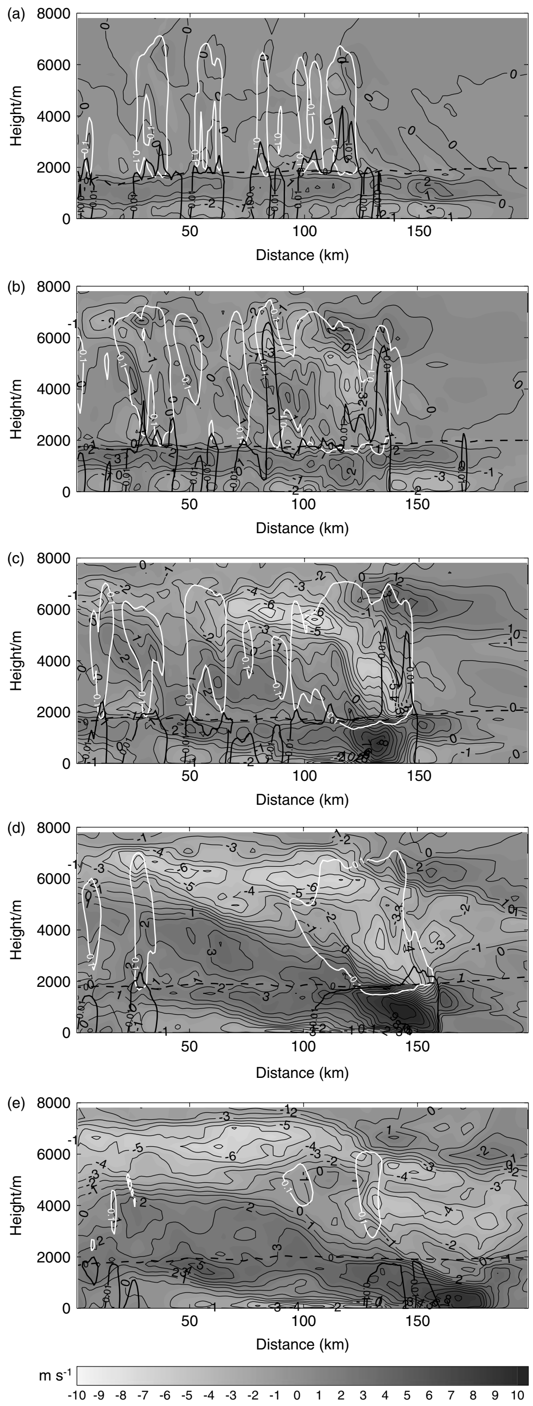

Figure 14. Vertical cross-sections from 1 km horizontal grid model forecasts at (a) 1000 UTC, (b) 1100 UTC, (c) 1200 UTC, (d) 1300 UTC, and (e) 1400 UTC: difference in horizontal wind speed along the direction of the cross-section between full model and reference run (shaded thin black contours at 1 m s^{-1} intervals), rain mixing ratio (0.01 g kg^{-1}, thick black contours), and total ice+snow mixing ratio (0.1 g kg^{-1}, white contours), both from the full model. Note that rain contour values are 10 times smaller than ice to allow for different order of magnitude of fall speeds. The dashed black line is the freezing level. The cross-section locations are as in previous figures.

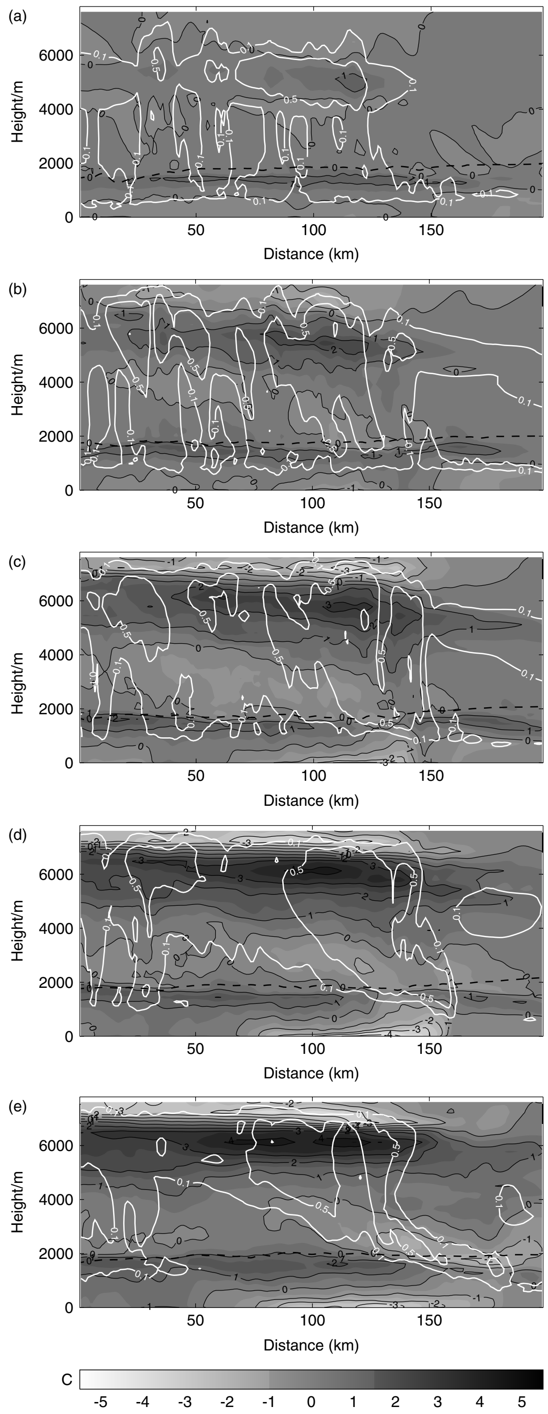

Figure 15. Vertical cross-sections from 1 km horizontal grid model forecasts at (a) 1000 UTC, (b) 1100 UTC, (c) 1200 UTC, (d) 1300 UTC, and (e) 1400 UTC: difference in θ between full model and reference run (shaded thin black contours at 1 °C intervals), full-model cloud fraction (white contours), and freezing level (dashed bold black line). Cross-section locations are as in previous figures.

when the leading edge has started to progress southeast of the 10.5 °C contour. By 1400 UTC, the gust front is at least 80 km to the southeast, though the remnants of the system at mid-levels are much closer. Thus, the initial line of convection essentially marks the leading edge of the region with very little convective inhibition – however, as the cold pool propagates perpendicular to this line it (and any mesoscale uplift) can lift incoming air, including this weak lid, thereby weakening it to the point where convection triggers.

The contribution of the modelled MCS to the flow has been found by subtracting equivalent cross-sections from the reference run from the model cross-sections from the run with full microphysics. The cross-sections in Figure 14 show the development of organised flows along the cross-section with an indication of the hydrometeor location. The potential temperature anomaly (i.e. difference from

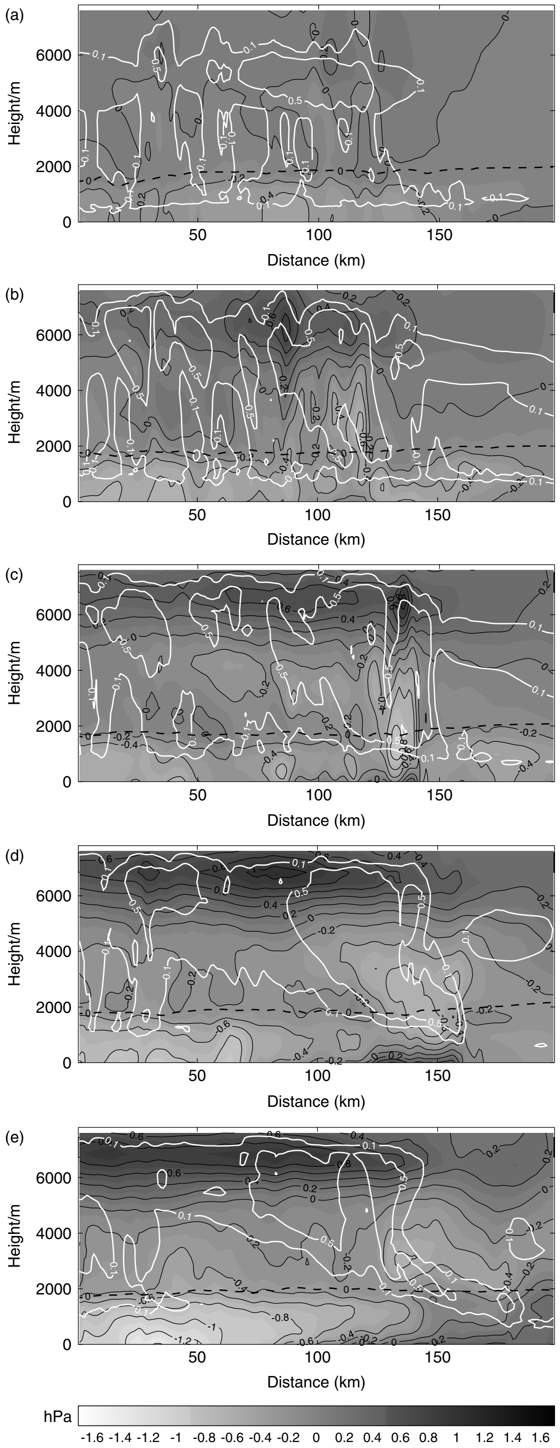

Figure 16. As Figure 15, but showing difference in pressure between full model and reference run (shaded thin black contours at 0.2 hPa intervals), full-model cloud fraction (white contours), and freezing level (dashed black line).

the reference) is shown in Figure 15 along with the total cloud fraction. We can also gain some insight by looking at the pressure anomaly (Figure 16). The component of wind perpendicular to the cross-section has been studied but is not shown; the only major features are upward transport of lower-momentum air (recall that the major component of shear is in this direction) and slight slowing down (a few m s^{-1}) in the cold pool.

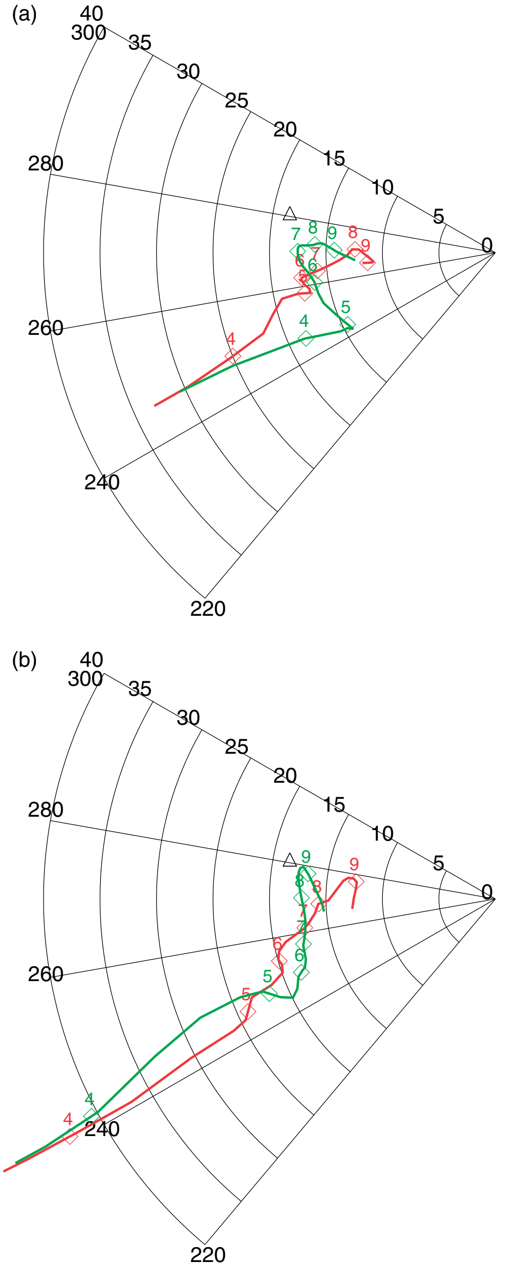

Figure 17. Hodographs of wind at 1300 UTC from the full model (grey, green online) and reference (black, red online) showing the average wind (a) from 70 to 120 km and (b) 160 to 180 km along the cross-sections in Figure 14(d). Pressure levels are marked with a numbered diamond every 100 hPa, labelled in hPa/100. This figure is available in colour online at wileyonlinelibrary.com/journal/qj

At 1000 UTC (Figures 14, 15 and 16(a)) there are essentially scattered cells up to the 130 km point along the cross-section (corresponding to the edge of the lid discussed above). The warm (1 °C), weak (1 m s^{-1}) 'jet' at about 1500 m corresponds to the difference in boundary-layer vertical mixing in the reference run discussed above, and should be considered an artefact of the method. The only other significant temperature difference is the beginning of a warm layer at cloud top, also peaking at about 1 °C and stretching about 50 km rearward. Though there may be some upper-level rearward advection at this stage (see the reference flow, Figure 13(a)), this warm anomaly presumably arises primarily from the merging of outflows from cells scattered behind the leading edge. The weak low-level negative pressure anomaly primarily reflects the heating difference in boundary-layer heating.

By 1100 UTC (Figures 14, 15 and 16(b)) the system has a clear dominant cloud line (at 100–130 km along the section), with some new cells ahead, slightly rearward sloping, with peak warm anomaly at its top (5–6 km) of about 2.5 °C. Beneath this (2–4 km) is the beginning of a cold anomaly (generally less than 0.5 °C) and there is a separate weak surface cold pool. Some cooling between is suggested by a weakening of the warm anomaly at the boundary-layer top. Slanting wind anomalies extending over about 50 km are associated with this cloud line; an ascending, rearward flow overlies a descending, forward flow at mid-levels (starting at 5 km) and there is a small forward cloud-top outflow.

The wind anomalies correspond broadly with the potential temperature anomalies, though the descending forward flow is a little higher than the top of the cold anomaly. A low-level jet is just beginning to become evident at the head of the main line (about 120 km along the cross-section) The dominant cloud line has a clear negative pressure anomaly at mid-levels (down to −0.4 hPa) and positive anomalies at cloud top and the surface. The same pattern is associated with the weaker cells behind the main system though with much less clear positive anomaly at the surface (which is still dominated by the shallow-cumulus negative surface pressure anomaly away from the main cloud).

By 1200 UTC (Figures 14, 15 and 16 (c)) this pattern has become dominant. The system is clearly organised with a low-level jet above 6 m s^{-1} relative to the reference flow close to its leading edge descending from about 4 km at least 75 km behind the leading edge, with evidence of intensification below the freezing level. This jet descends beneath a rearward slantwise flow ascending from mid-levels (3–4 km) to 7 km, with upper-level rearward flow reaching 6 m s^{-1} along the cross-section. The surface jet is at the head of a cold pool generally below 1 km extending 75 km behind the gust front. The cloud and hydrometeor distributions show a line of intense, essentially vertical, mixed-phase cells above the gust front, with rain falling from near cloud top. Ice cloud extends more than 40 km behind this with little or no rain above the melting layer. The multi-cellular nature of the system is evident in the mean cross-sections (and, of course, even more so in the individual cross-sections) as distinct (but weaker) cells exist behind the line of cells along the front.

The peak warm anomaly (3 °C) is well behind the leading edge, the mid-level cold anomaly covers much of the area to the rear of the leading edge, and the surface cold pool is well established, with a characteristic ‘nose’ at the gust front. Note that, although there is some complication added to interpretation by the boundary-layer top warm anomaly, judging by the size of this elsewhere these two cold anomalies appear to be distinctly different at this stage. A cold anomaly also exists at cloud top, presumably a combination of evaporative cooling by mixing with tropopause air, long-wave radiative cooling, and possibly large-scale lifting of the tropopause.

The leading-edge upright convective cells produce a strong negative pressure anomaly from close to the surface to 4 km (peak −0.8 hPa), and a general mid-level negative pressure (−0.3 to −0.4 hPa) anomaly extends behind the system beneath the cloud-top positive anomaly with a negative pressure anomaly behind. The surface cold pool produces a positive anomaly for 20–30 km behind the leading edge. Note that this is consistent with the observations in Part 1 which show peak positive pressure anomalies some distance behind the gust front; however, it also suggests that the surface pressure anomaly is not solely the result of the cold pool (as suggested by e.g. Droegemeier *et al.*, 1987).

By 1300 UTC (Figures 14, 15 and 16(d)) the pattern is similar except it is larger, more intense, and the gust front and cold pool are showing signs of overrunning the main system, with less evidence of upright convection at the leading edge. The system extends over 100 km front to back and the cold pool is more intense. The precipitation is confined to a band about 40 km behind the gust front, and there is a broad precipitation-free zone for about 80 km behind this. The first showers behind appear to coincide with the rear edge of the cold pool (as well as orographic uplift).

At earlier stages it was not obvious that the rear-inflow jet beneath the stratiform region and the low-level jet at the head of the cold pool were contiguous. However by 1300 UTC, the two much more clearly show a downward-sloping rear to front flow. While it is difficult to identify a ‘start’, the rear-inflow jet is apparent from about 150 km behind the leading edge, almost as far back as the upper-level outflow. Though it does show some structure (complicated by the boundary layer in the reference discussed above), it is broadly contiguous with the low-level jet, which is reaching 10 m s^{-1} relative to the reference flow close to its leading edge. The low-level jet is now also slanting down to the surface, suggesting some contribution from slantwise descent. There is a weak mid-level rearward inflow from ahead of the system. Presumably because of the overrunning cold pool, the negative pressure anomaly from the leading edge upright convection is now separated from the surface and the positive anomaly has fully undercut. At the rear of the system, as well as a mid-level negative pressure anomaly, there is a strengthening negative surface anomaly behind the cold pool.

By 1400 UTC (Figures 14, 15 and 16(e)) the leading edge of the low-level jet has advected about 50 km ahead of the mid-level cloud, and there are no deep cells above the leading edge. (We have not shown cross-sections of vertical velocity for reasons of space, but they are consistent with the slantwise ascent and descent discussed above). Both the overrunning cold pool and mid-level rearward inflow are very clear; interestingly, the mid-level cold anomaly has also run ahead of the main system beneath the midlevel rearward inflow, as has the mid-level negative pressure perturbation.

The system can be described as most organised around 1200 to 1300 UTC. Figure 17 shows mean wind profiles behind the upright convection part of the system (i.e. the stratiform part) and ahead, compared with the reference profiles. The stratiform region clearly shows the weak rear-inflow jet, peaking at about 700 hPa, and a sharp shear layer separating it from the rearward upper-level outflow at 500 hPa and above. Ahead of the system is the leading edge of the cold pool at 900 hPa. Above 500 hPa is a weak forward outflow; between the two, from 700 to 500 hPa, is a weak mid-level inflow. Thus, as discssed above, the system has developed a (relatively weak) cross-shear structure which is essentially typical of trailing stratiform systems. Given the strong shear, the development of rotation in the system is not especially evident (beyond that required to evolve the shape of the system from its initial linear form). Examination of the vertical component of relative vorticity shows a great deal of small-scale structure originating from the convective plumes, but when averaged a clear structure does appear; averaging from 70 to 160 km along the average cross-sections shows the development of cyclonic relative vorticity between the surface and 4 km, peaking at 2 km, with a peak at 1300 UTC of about $10^{-4}\,\mathrm{s}^{-1}$, and anticyclonic relative vorticity above with similar magnitude. The anticyclonic vorticity peaks at about 4.5 km and again (somewhat larger) at 7 km.

We have examined the origins of air in various parts of the system. The first point to note is that, given the 3D evolving nature of the system, it is difficult to uniquely define a system propagation speed. Second, the along-line shear means that all trajectories changing height tend to be dominated by along-line motion. By 1300 UTC the cross-line component reflects the general structure discussed by the review of Houze (2004) for trailing stratiform systems; in particular, much of the air in the rearward slantwise ascent originates at mid-levels (as found by Cotton *et al.*, 1995), and there is thus evidence of overturning of the inflow air, with some trajectories passing through the convective line with only weak ascent. However, some caveats must be applied to this conclusion; calculating trajectories in the presence of strong convective plumes is challenging – it is likely that numerical mixing takes place, at least in part, due to model discretization errors. A better approach might be to follow tracers through the model integration but, even then, spurious numerical diffision is inevitable to some degree. Finally, it should be noted that, as pointed out by Pandya and Durran (1996), the extent of the trailing stratiform region is not determined by advection of air backwards, and many trajectories show relatively little horizontal displacement over a few hours.

Some acceleration of the system as a whole occurs associated with strengthening of the cold pool and development of the weak rear-inflow jet. The propagation speed based on the change in the position of the leading edge of precipitation along each line over 1 h is about $12\,\mathrm{m\,s^{-1}}$ (a general acceleration occurs after 1300 UTC – section 5 – so the precise speed depends upon the averaging period chosen). The peak speed along the cross-section in this jet is somewhat faster, approximately $16\,\mathrm{m\,s^{-1}}$ at 1200 UTC and $18\,\mathrm{m\,s^{-1}}$ at 1300 UTC.

In summary, the system exhibits a propagating and strengthening cold pool which propagates with the leading edge of the system for a few hours, a largely rearward-sloping and rearward-flowing upper-level anvil region and a downward-sloping rear-inflow jet associated with cooling beneath the upper-level cloud. The leading edge of the cold pool can force ascent and trigger convection and, in addition, any cells which trigger ahead of but close to the system (by sea-breeze convergence, elevated surface heating over hills or gravity-wave propagation ahead of the system) are caught up with and subsumed into the system. The system becomes more sloping with time, and the surface cold pool accelerates ahead of the region of greatest instability and under (or into) the 'lid'. This coincides with propagation over the sea, which both aids the acceleration by reducing the low-level system-relative inflow, and reduces the instability of the low-level air, thus rapidly reducing the convection at the leading edge. Over land, the system continues to overtake cells triggered ahead, and thus maintains intense, leading-edge precipitation.

When considering the mechanism for rear-inflow jet production, the buoyancy and pressure distributions are very consistent with the conceptual model of Weisman (1992). Broadly, the horizontal buoyancy gradient at the leading edge of the cold pool and upward transport of air with rearward momentum relative to the system is largely responsible for the rearward development of the system, while the mid-level low-pressure anomaly (or, equivalently, upper-level rearward warm anomaly) leads to acceleration into mid-levels from behind and (to some extent) in front. They also strongly resemble the gravity-wave results of Pandya and Durran (1996), though their article does not include the impact of along-line shear on the gravity-wave propagation. For the first few hours, at least, the rear-inflow jet and cold pool seem to be separate flows (albeit with some mechanistic connection) but by 1400 UTC it would appear that the downward-sloping rear-inflow jet is helping to feed the cold pool with cooled air from mid-levels. This is also consistent with the results of Pandya and Durran (1996) which suggest that the modification of low-level stability by the cold pool may be necessary to modify the gravity-wave response in the region of the downward-sloping rear-inflow jet. At this level of comparison, we are not suggesting that the viewpoints of Weisman (1992) and Pandya and Durran (1996) are mutually exclusive. The former primarily argues in terms of the vorticity equation, the latter in terms of gravity-wave dynamics. The main point of departure is that Pandya and Durran (1996) show that diabatic heating in the trailing stratiform region modifies, but is not essential for, the generation of the rear-inflow jet.

5. Model sensitivity to precipitation microphysics

In order to identify the main factors driving the development and propagation of the system, especially the cold pool and the rear-inflow jet, we have rerun the model with a number of changes to the parametrized physics. As noted above, the choice of parameters used in the single-moment scheme is a compromise. It is likely that a higher-order scheme would have a significant impact on the development of an MCS, as both convective and stratiform regions are important and are likely to have markedly different microphysical properties. However, the objective here is to study gross effects of including, for example, ice processes at all, rather than the more subtle impacts of changing size spectra. Similar experiments have been performed by others (e.g. Schumacher, 2009), though we are not aware of similar experiments applied to a parallel stratiform system.

The results are briefly summarised in Figures 18, 19 and 20, which show the same averaged cross-sections at 1300 UTC as shown in Figures 15(d), 14(d) and 16(d), which will be described as the 'standard' run. These 'standard' cross-sections are repeated in each figure to facilitate comparison. This time represents the system at its strongest 'upright' phase, with the first signs of the cold pool accelerating ahead of the mid-level flow.

5.1. *Single prognostic ice phase*

Figures 18(b), 19(b) and 20(b) show results using the single prognostic ice phase with diagnostic split between ice and snow as used operationally by the Met Office (at the time of writing). As suggested in section 2, the results are extremely similar to those from the standard run. There are subtle differences. There is more cloud at the top of the leading edge as, presumably, more ice can be transported

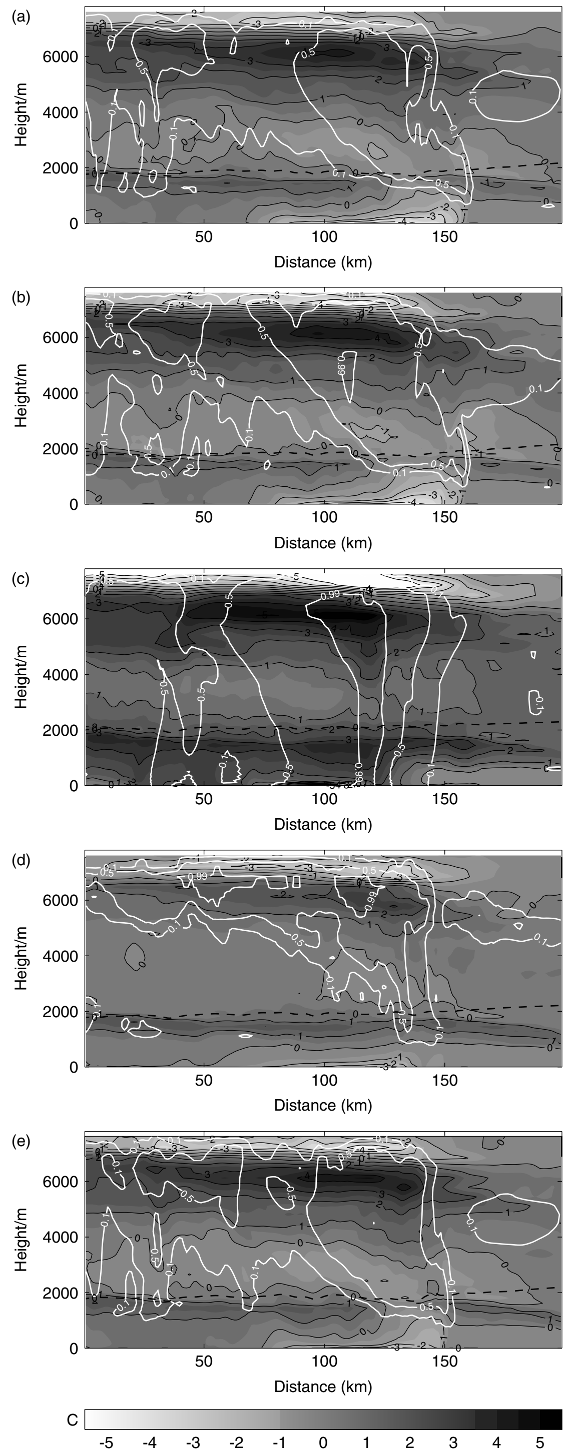

Figure 18. Vertical cross-sections from 1 km horizontal grid model forecasts at 1300 UTC showing difference in θ between the sensitivity run and the reference run (shaded thin black contours at 1 °C intervals), model cloud fraction (white contours), and freezing level (dashed black line). Sensitivity runs are (a) full microphysics, (b) single (combined) prognostic ice phase, (c) no cooling, (d) no ice processes, and (e) no rain evaporation from model.

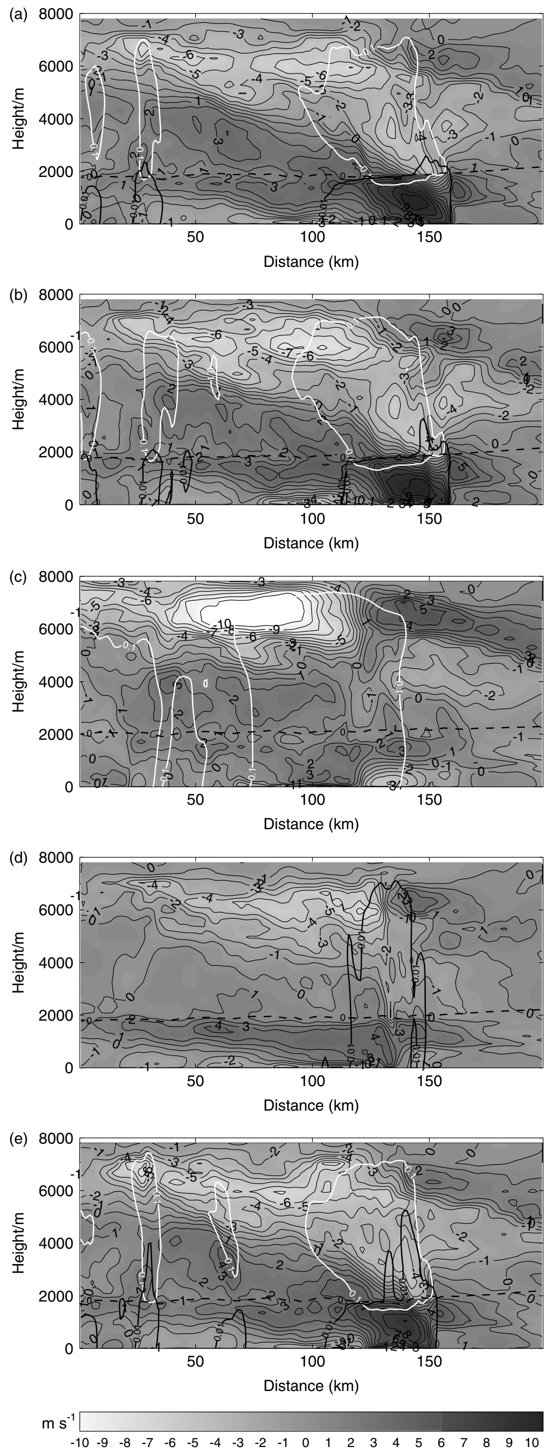

Figure 19. As Figure 18, but showing difference in horizontal wind speed along the direction of the cross-section between full model and the reference run (shaded thin black contours at 1 m s^{-1} intervals, rain mixing ratio (0.01 g kg^{-1} contour, bold black), and total ice+snow mixing ratio (0.1 g kg^{-1} contour, white). Note that rain contour values are 10 times smaller than ice to allow for different order of magnitude of fall speeds.

forward of the updraught. The 'anvil' cloud appears a little more organised, the cloud-top warm anomaly is a fraction of a degree stronger to the rear, and the cold pool is slightly different. These differences are certainly unverifiable, and may not be systematic since similar differences could certainly be generated by small perturbations (Leoncini *et al.*, 2009).

5.2. *No cloud and precipitation diabatic cooling*

Figures 18(c), 19(c) and 20(c) show the impact of turning off all diabatic cooling processes due to cloud and precipitation. This includes the impact of cloud on radiation but not that of rain or snow on soil moisture or surface exchange. Including or not either of these processes does not change the qualitative behaviour, but they do introduce shallow surface cooling associated with cloud or rain which may resemble a weak cold pool at the surface (1–2 °C in the case of radiative forcing), though with generally very much smaller depth. This run also includes turning off the melting process, so most precipitation falls as snow. Perhaps surprisingly, in this case, a line of convective cloud does form. A broad band (corresponding roughly to Lines A and B identified in Part 1) develops at 1000 UTC. This band develops widespread, deep convective showers and propagates eastward with a well defined southeast edge but widespread precipitation behind due to the lack of evaporation and melting of snow from the anvil. By 1300 UTC, a band of showers exists about 30–40 km behind the standard-run squall line.

Figure 18(c) shows that, as expected, there is only a very shallow layer of surface cold air associated with the showers, associated with the impact of snow on surface exhange. The upper-level anvil warming is very similar to the standard run (where there is cloud) but the cooling at cloud top rather larger. Note that this is not radiative cooling, but presumably the dynamical (primarily gravity-wave) response to the changed heating profile. The boundary layer is warmer due to the absence of cooling by evaporation and melting. Figure 19(c) shows a weak low-level convergence line associated with the line of showers about 40–45 km behind the reference-run gust front; both the cross-sections and examination of the surface temperature and wind suggest that this may be due to a low-level flow off the sea which is probably largely thermally driven with some contribution from land–sea roughness contrast. However, the long-lived nature of this shower band, and its orientation, are consistent with the progression of the rearward edge of the lid and the forward edge of the upper-level low-θ_s air discussed in section 3.

There is a weak near-horizontal mid-level rear-inflow jet at about 4 km and the system-relative rearward outflow above this is significantly stronger than in the standard run. The rear-inflow jet is presumably driven by the positive buoyancy in the rearward upper-level outflow, as discussed by Weisman (1992). Figure 20(c) shows a strong pressure perturbation with a simple pattern associated with the cloud, going from a negative surface perturbation down to about −2 hPa to a positive perturbation up to 1.4 hPa close to cloud top. Ahead of the cloud there is significant mid-level warming, slightly more than the standard run, and a slantwise pattern to the mid-level rearward flow and upper-level forward flow similar to the standard run.

Unlike the other runs, there is also a surface inflow of up to 2 m s^{-1} ahead of the system. This becomes established between 1000 and 1100 UTC and is a feature throughout the simulation. This is presumably driven by the negative surface pressure perturbation.

It is interesting to note that the 12 km model also produces no cold pool, but does produce a broad propagating band of parametrized convection in a very similar location, consistent with this band corresponding to the region of strongest large-scale convective forcing.

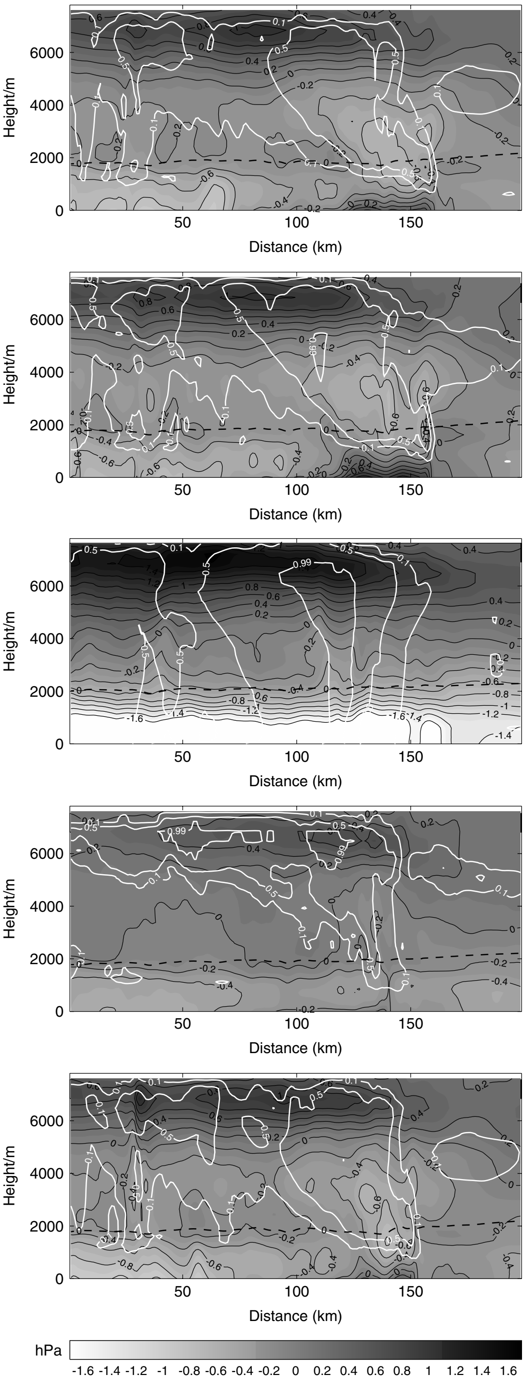

Figure 20. As Figure 18, but showing difference in pressure between full model and reference run (shaded thin black contours at 0.2 hPa intervals), full-model cloud fraction (white contours).

5.3. No ice-phase processes

Figures 18(d), 19(d) and 20(d) show the impact of turning off just the ice processes in the model (so rain can form only through warm coalescence and accretion processes). In this case, a very distinct line of showers also eventually forms. A shallow cold pool does still form, with a distinct low-level jet and gust front. This front is about 15–20 km behind the standard-run gust front and significantly weaker than in the full microphysics run, but further to the rear the low-level jet is only a little weaker. Note that the extent of the low-level jet to the rear of the system is somewhat exaggerated by the nature of the reference run; winds between about 1 and 2 km are somewhat slower in the reference since shallow cumulus or stratocumulus mixing is absent. (This is evident in all runs but clearest here).

A distinct (liquid) anvil exists behind the line of showers associated with a region of weak (system-relative) rearward flow (the cloud base is around 3.5 km, just below this region), but there is no (or only an extremely weak) distinct rear-inflow jet, consistent with the much-reduced warming in the anvil region due to the absence of glaciation and much reduced (or absent) evaporative cooling from precipitation below the anvil.

The pressure perturbation shows a weak upper-level positive anomaly (up to about 0.4 hPa) and low-level negative anomaly (down to −0.4 hPa) with a very weak surface positive anomaly associated with the cold pool (close to zero, but noticeable as a positive perturbation to the negative surface anomaly behind). The absence of a strong surface pressure positive anomaly is consistent with the absence of the deep cold pool at the front of the system, which results, at least in part, from melting above. Above this, the weakened negative anomaly presumably arises from weakening of the diabatic warming and of the resulting updraughts.

The linear form actually resembles well the early linear form of the observed system, consistent with the idea that the early linear form is primarily controlled by the edge of the lid with some organisation from the local surface cold pools associated with rainfall and the direction of wind shear before internal dynamical processes start to drive the system. The showers are fewer in number than in the reference run, but somewhat more intense (about double the peak intensity) and have less light rain accompanying them.

5.4. *No rainfall evaporation*

Figures 18(e), 19(e) and 20(e) show the impact of turning off just the rainfall evaporation. This has relatively small impact on the overall system, but it does markedly reduce the strength and propagation of the cold pool compared with the standard run. The cross-section at 1300 UTC without evaporation of rain actually resembles that in the standard run at 1200 UTC, though the peak wind speed is at a slightly higher altitude in the no-evaporation run, suggesting the evolution is similar but slower. Examination of the mean cross-section and individual cross-sections suggests that, in the absence of rainfall evaporation, the low-level jet remains a few kilometres behind the region where warm rain processes dominate, suggesting that melting of snow is the main process driving the remaining low-level jet. Direct evaporation of rain provides further cooling but also, perhaps importantly, can provide cooling closer to the leading edge of the system, via warm-rain processes, than processes acting via the ice phase. However, it is difficult to separate processes further: turning off melting is feasible, but would leave snow falling through a sub-saturated environment above freezing, leading potentially to very rapid sublimation.

5.5. *Cold pool propagation*

Changes to the cloud microphysics produce clear impacts on the surface cold pool and on the propagation of its leading edge along the cross-section. An objective method has been used to define this; in most cases the location of the maximum absolute gradient in perturbation wind speed has been used. In the 'no-cooling' case this fails, so the furthest point along the cross-section with mean cloud fraction at 1280 m greater than 0.4 or low-level rainfall concentration greater that 0.065 kg kg^{-1} has been used. This criterion gives the same result (within 1 km) as the wind speed gradient in other cases. All the results agree with a subjective assessment, though there is some ambiguity about what should be taken as the leading edge at 1000 UTC; essentially we have taken the position of the furthest edge of the cells along the cross-section.

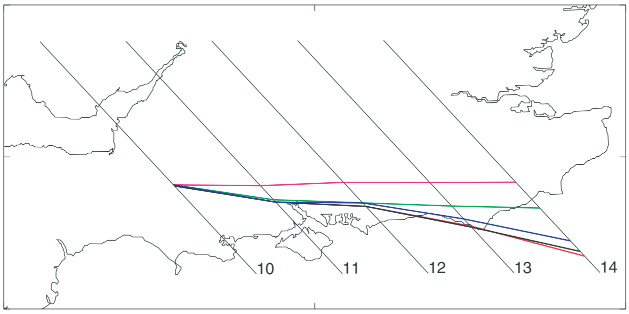

Figure 21. Position of the gust front along each cross-section for different model runs. From the northernmost: no cooling, no ice phase, no rainfall evaporation, full microphysics, single ice phase. The time (UTC) of each cross-section is marked. This figure is available in colour online at wileyonlinelibrary.com/journal/qj

The positions derived are shown in Figure 21. The cross-section positions were chosen to show the broadly eastward movement of the system as a whole and individual cells with the mid-level flow. The gust front is approximately perpendicular to each cross-section and we shall concentrate on the component of the propagation along the cross-section direction. The 'no-cooling' case essentially moves due east, with a slight northward tendency which may be an artefact of the choice of cross-section positions. All other runs propagate along the cross-sections to varying degrees.

All runs jump forward between 1000 and 1100 UTC, reflecting the formation of cells ahead of the line which do not form in the no-cooling case. They then propagate more steadily, with acceleration in the later stages, the no-ice run slowest, followed by the no-rain-evaporation run, with the full microphysics and single-ice runs essentially giving the same result. As noted above, the no-cooling case (not shown) develops a rearward-sloping front-to-back flow between 1000 and 1100 UTC, sooner than the other runs, and a weak but noticeable surface inflow from ahead of the system, which presumably contributes to the absence of triggering ahead of the system. Thus, one can say that the diabatic cooling contributes to the triggering ahead of the system, not particularly by forcing ascent ahead of the system, but by inhibiting the low-level inflow that would otherwise occur.

It is of interest to see if the propagation speed along the cross-section is related to the cold-pool strength. A measure of the cold-pool strength has been derived from the vertical integral of buoyancy compared with the reference (no-cooling) run (e.g. Benjamin, 1968; Simpson, 1987):

$$Vp = \left(g \int \frac{\Delta\theta_{\mathrm{v}}}{\overline{\theta_{\mathrm{v}}}}\,\mathrm{d}h\right)^{\frac{1}{2}}. \qquad (1)$$

(Note that this does not include a factor of 2.) As discussed in Part 1, numerous authors have extended this theory, but generally the cold-pool buoyancy appears as a velocity scale in the above form, and the main objective is to look for correlation, not quantitative prediction. This has been computed as an average over 50 km behind the leading edge of the MCS, though other averaging choices (e.g. averaging over just 10 km, or averaging ±10 km either side of the minimum surface temperature) give qualitatively similar results. Figure 22(a) shows this velocity scale plotted as a function of the distance the leading edge of the MCS has reached along the cross-sections relative to the 'no-cooling' case. The points are at hourly intervals from 1000 to 1400 UTC, with the assumption that the systems are co-located at 1000 UTC. The times are not marked, but in all cases the displacement increases monotonically with time. In all cases the system propagates ahead of the 'no cooling' reference case and the cold-pool strength increases with time until the 1300–1400 UTC period where the MCS leading edge accelerates in the standard and 'no rain evaporation' cases, and somewhat earlier in the single ice-prognostic case. As noted above, this corresponds roughly with propagation over the sea, though the ≈100 m high hills of the South Downs near the south coast may also have formed a barrier to the flow.

These data have been used to estimate the component of propagation speed in the direction of the cross-sections (relative to the movement of the cross-sections) using a simple linear differencing (Figure 22(b)); for consistency, the cold-pool speeds in Figure 22(a) have been averaged to the half hour in Figure 22(b) (so the last point in each curve shows the average of Vp evaluated at 1300 and 1400 UTC, plotted against the distance (m) ahead of the 'no-cooling' case at 1400 UTC minus that at 1300 UTC, divided by 3600 s). Note that, given the multi-cell nature of the system and the uncertainty in precisely fixing the leading edge, these data have significant error, especially the earlier data points (probably 1–2 m s^{-1} in the propagation speed), though relative comparisons are more accurate (because while the precise location of the leading edge may be uncertain, in most cases it is clear that one model configuration is ahead of another).

The results are somewhat paradoxical. The three runs with ice processes all show a fairly consistent correlation between propagation and cold-pool strength, especially when one considers that the final points involve propagation over the sea. This suggests propagation is strongly related to cold-pool strength (as suggested by Rotunno *et al.* (1988) and later work discussed in Part 1). However, the no-ice case shows a low propagation speed, similar from 1100–1200 and 1200–1300 even though it clearly develops a strengthening cold pool. The 'no rain evaporation' case propagates significantly more, and does suggest correlation between propagation and cold-pool velocity scale. However, the values of Vp are only a little more than the 'no ice' case, which suggests that this correlation may be fortuitous. The full microphysics and single-ice cases are essentially the same. Both Vp and actual propagation speed are greater than in the 'no rain evaporation' case, consistent with proportionality between the two.

The situation is, no doubt, complicated by the fact that the systems are developing rapidly with time; arguably, the cold-pool velocity scale data are a little more consistent with the propagation speed if the propagation speed is plotted against the cold-pool velocity scale in the previous hour (i.e. assuming some lag between cold-pool formation and propagation), but it is difficult to avoid the conclusion that the no-ice case has a cold pool not very different in general from the 'no rain evaporation' case but it propagates significantly slower after 1200 UTC when the systems are well organised. There *is* a difference in the cold pool at the leading edge; as noted above, the deeper cold layer and its associated positive pressure anomaly is absent, as is the mid-level negative anomaly associated with the convective cells, and also the weak mid-level inflow. A combination of factors probably cause these differences, and it is difficult to separate them, but the absence of melting in the no-ice case is probably a major factor at the leading edge.

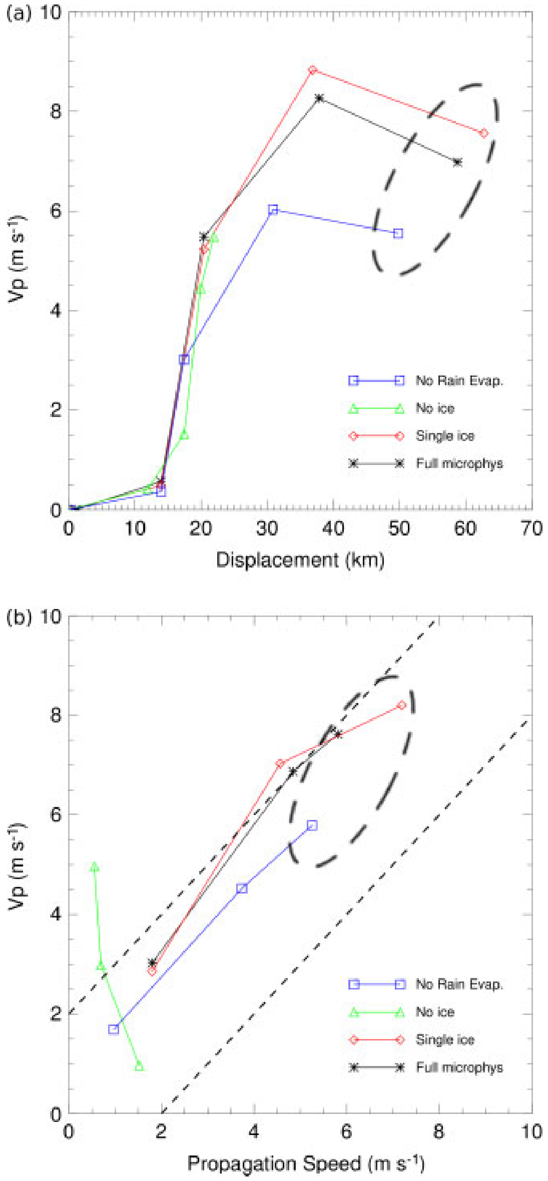

Figure 22. Cold-pool velocity scale (a) as a function of displacement distance of the leading edge of the MCS along the cross-sections above ahead of the 'no cooling' case, and (b) as a function of the component of propagation speed of the leading edge of the MCS along the cross-section direction. In (b), the cold-pool velocity scale increases monotonically with time and data points are from 1100–1200, 1200–1300 and 1300–1400 UTC. Dashed lines are gradient=1 reference lines, and dashed ellipses emphasise points where the leading edge is entirely over the sea. This figure is available in colour online at wileyonlinelibrary.com/journal/qj

When considered as a whole, there does appear to be a correlation between propagation speed and cold-pool strength, especially if we assume that the propagation over the sea would be expected to be greater than over land for a given cold-pool strength. It must be remembered that here we are discussing propagation of the low-level gust front, which clearly eventually runs ahead of the mid- and upper-level cloud. However, the lack of propagation in the 'no ice' case suggests that, at least for the early lifetime of the system, the cold pool does not drive the propagation speed, but rather the reverse; the cold pool is partially the result of precipitation and spreads with the leading edge of the precipitation, but its strength also reflects the propagation of the system which is primarily driven by the positive buoyancy in the upper level of cloud. The weak rear-inflow jet that develops as a result promotes the evaporation of cloud and snow below the anvil, as well as transporting snow forward before it melts, and thus helps to form the surface cold pool. This is further augmented, mainly at the leading edge, by rainfall evaporation and mainly serves to suppress convection to the rear of the system until it has grown strong enough (or the local environment changes by advection over the sea) to propagate ahead of the system, eventually destroying the system organisation. The cold pool does not necessarily propagate with the system, but rather grows as the system propagates. However, it does serve to sharpen the leading edge of the system in terms of temperature, wind (i.e. there is a gust front) and the triggering of new cells. Eventually the cold pool does become strong enough or the environment changes enough to enable it to propagate with and then ahead of the system.

In the no-ice case, only very weak propagation occurs because of the weaker diabatic heating in the upper-level cloud, and no cooling occurs below the anvil. A cold pool does form driven by rainfall evaporation at the leading edge, so this propagates with the system and helps maintain a contiguous linear leading edge. The absence of glaciation promotes more 'warm' rain production in the convective towers at the leading edge, helping strengthen this cold pool.

A quantitative analysis has been attempted of the rear-inflow jet and mid-level cooling at the rear of the system. However, this is complicated by the variable morphology of the system, rendering it difficult to compare like with like. The results obtained essentially confirm but do not add to observations discussed above, that the three cases with cooling by ice processes all develop very similar rear-inflow jets and heating and cooling patterns to the rear of the system. The 'no cooling' case also develops a weak rear-inflow jet but this is substantially weaker as it approaches the leading edge of the system. The 'no ice' case develops no significant jet descending from mid-levels.

In summary, model sensitivity studies show that a propagating, linear band of convection would have formed in the absence of diabatic cooling, driven by the location and orientation of the low-level lid and upper-level instability. Warming in the largely rearward-sloping anvil cloud is substantially enhanced by the latent heat released by ice formation. The downward-sloping rear-inflow jet feeding the surface cold pool is produced by the diabatically heated anvil and enhanced by evaporation of hydrometeors below the anvil. Both mechanisms are greatly enhanced by ice-phase processes (condensation within and evaporation and melting below the anvil). The weak rear-inflow jet appears largely responsible for the slow propagation of the system. Diabatic cooling from microphysics generates the surface cold pool which intensifies and grows in extent with time. The surface cold pool is enhanced by evaporation of rain, especially from new cells at the leading edge, and in their absence a much weaker and a smaller surface cold pool results from evaporation of rain. There is evidence in the model runs of a transition from a mainly upright system in its early stages to one driven strongly by slantwise ascent and descent as microphysical cooling from the anvil has time to have greater impact on the system dynamics and, at the latest stages, there is some evidence of mid-level inflow from ahead of the system.

6. Summary and conclusions

The detailed observations of the developing MCS over southern England on 25 August 2005 made available by the CSIP project and their analysis described in Part 1 have enabled a detailed validation of simulations using the MetUM at 1 km horizontal grid spacing and 76 vertical levels. Overall, the development of the system is simulated remarkably well. Though the early organisation of the system is not especially well treated, a substantial cell initiated at approximately the right time and place and this went on to form a system which developed qualitative and quantitative features very similar to the observations described in Part 1.

As suggested by the analysis of Part 1, the broad structure of the system and its evolution broadly matches linear systems summarized by Houze (2004), in particular the parallel stratiform systems of Parker and Johnson (2000) and Parker (2007a). The initial linear system is aligned with the mid-level wind shear. As suggested by Parker (2007b), the initial linear form is also promoted by other features, in this case possibly the coast but primarily the rearward edge of a weak, inhibiting 'lid'. The system rapidly develops a cold pool which promotes propagation perpendicular to the initial line and development of a more trailing stratiform structure.

The position and propagation speed of the system is well reproduced; at early stages the system velocity is dominated by ambient mid-level advection, not only of the convective cells, but the rearward edge of the 'lid', the position of which was remarkably well forecast. In the early stages, there is some discontinuous propagation as new cells form ahead of the initial line. The surface cold pools rapidly coalesce so that by 1200 UTC the leading edge of the cold pool is propagating with the system. Some acceleration of the system as a whole occurs associated with strengthening of the cold pool and development of the weak rear-inflow jet. As the system becomes more sloping, the surface cold pool eventually accelerates ahead of the region of greatest instability and under (or into) the 'lid'. This coincides with propagation over the sea, which both aids the acceleration by reducing the low-level system-relative inflow, and reduces the instability of the low-level air, thus rapidly reducing the convection at the leading edge. Over land, the system continues to overtake cells triggered ahead, and thus maintains intense leading-edge precipitation.

Changes to the microphysics scheme have provided some insight into the dominant mechanisms operating in the model. A run with no diabatic cooling in the microphysics forms a useful reference; it demonstrates that a linear system forms without the presence of a surface cold pool (in some ways similar to Trier *et al.*, 2011). This system propagates with the edge of the 'lid' and remains linear because of the rearward advection of the upper-level cloud and associated warm anomaly and the gravity-wave response to the convective heating (Pandya and Durran, 1996) though mid-level convergence may also play a role (Crook and Moncrieff, 1988). The initial discontinuous propagation is absent; new cells do not form ahead of the system in the absence of diabatic cooling because the cooled air near the surface weakens and eventually reverses the sign of the surface low pressure which otherwise drives a low-level inflow from ahead of the system. Thus, although a propagating line forms with no cloud microphysical diabatic cooling processes, these are essential to capture the system velocity for both the discontinuous and later continuous propagation of the system. Thus, propagation is not through a direct coupling between tropospheric gravity waves and diabatic heating, as discussed by many authors including Raymond (1984), Schmidt and Cotton (1990) and Cram *et al.* (1992) though, of course, diabatic cooling might further enhance a gravity wave with the appropriate vertical structure. Likewise, the initial discontinuous propagation seems not to be the direct result of short-wavelength gravity waves generated by the convective heating, as discussed by Fovell *et al.* (2006). Though gravity waves would, of course, be generated by the system, there is no clear trapping mechanism in the environmental profile.

Ice-phase processes greatly enhance the development of the system. The warming in the rearward-sloping anvil is enhanced by latent heating due to ice formation. This enhances the rear-inflow jet, promoting the system propagation. These are further enhanced by ice evaporation and melting under the rearward-sloping anvil, which drives the surface cold pool formation, with only a minor contribution at the leading edge from rainfall evaporation. The formation of the weak rear-inflow jet seems largely driven by the presence of slow-moving, warm air in the upper-level front-to-rear outflow; we have not attempted to distinguish between the mechanisms of Weisman (1992) (horizontal vorticity generation by the horizontal buoyancy gradient), 'flow-blocking' (Schmidt and Cotton, 1990), and gravity-wave response to diabatic heating and cooling (Pandya and Durran, 1996). In the second case, the dominant mechanism seems to be the downward deflection of ambient flow in a sheared environment (not a strong feature here as the convective line is initially along-shear), whereas in the first case a degree of horizontal acceleration also occurs. The Weisman (1992) view is not broadly inconsistent with the gravity-wave response, in that its vorticty equation view is largely applicable to gravity-wave response to buoyancy production – the main difference being the relative importance of advection. In our case, the flow is so weak it would be difficult to distinguish the mechanisms.

The development of a more slantwise system with time is consistent with the rearward upper-level flow, but this is enhanced by the development of a mid-level inflow from ahead of the system, presumably generated by the negative mid-level pressure anomaly in the core of the system. This is partially associated with the vertical convective cores but as the system develops it becomes clearly associated with a contiguous sloping updraughts starting tens of kilometres ahead of the system. This suggests the beginning of a transition to balanced dynamics (Raymond and Jiang, 1990; Cotton *et al.*, 1995; Olsson and Cotton, 1997).

Details of the microphysics scheme (insofar as they have been tested) only make minor changes to the system development, though the single-prognostic ice phase scheme used operationally in the Met Office may provide marginally superior results in terms of slightly greater system propagation speed and cold-pool strength compared with the three-prognostic ice scheme. This probably indicates compensating errors, as the system is initially slower to organise than observed.

The cold-pool strength is broadly correlated with system propagation, as suggested by Rotunno *et al.* (1988), but sensitivity studies suggest that, at least during the transition period (1100–1300 UTC), the cold pool strengthens as a result of the system development rather than *vice versa*, including a more rearward-slanted mesoscale updraught and strengthening of the weak rear-inflow jet. The cold pool does contribute to maintaining a sharp leading edge. In part, the leading edge of the cold pool can force ascent and trigger convection and, in part, any cells which trigger ahead of but close to the system (by sea-breeze convergence, elevated surface heating over hills or gravity-wave propagation ahead of the system) are caught up with and subsumed into the system. Eventually, however, aided by changing ambient conditions over the sea, the cold pool attains enough strength to 'break free' and propagate ahead of the mid-level cloud in a manner consistent with density-current-based theories.

Acknowledgements

The authors would like to acknowledge the Natural Environment Research Council (NERC) and the Met Office National Meteorology and Public Weather Service Programmes for funding CSIP. We would like to thank all who took part in the CSIP observational campaign. We also are grateful to the Met Office and NCAS CMS for provision and support of the MetUM and Eumetsat and the Met Office Autosat team for Meteosat-8 data. The Chilbolton Laboratory is managed by John Goddard and owned by the Council for the Central Laboratory of the Research Councils. Finally we would like to thank the reviewers of earlier forms of this article, one anonymous, the others Bill Cotton and Russ Schumacher, for their helpful and constructive comments which we believe have very significantly contributed to this article.

References

Atlas D, Tatehira R, Srivastava RC, Marker W, Carbone RE. 1969. Precipitation-induced mesoscale wind perturbations in the melting layer. *Q. J. R. Meteorol. Soc.* **95**: 544–560.

Benjamin TB. 1968. Gravity currents and related phenomena. *J. Fluid Mech.* **31**: 209–248.

Browning KA, Blyth AM, Clark PA, Corsmeier U, Morcrette C, Agnew JL, Ballard SP, Bamber D, Barthlott C, Bennett LJ, Beswick KM, Bitter M, Bozier KE, Brooks BJ, Collier CG, Davies F, Deny B, Dixon MA, Feuerle T, Forbes RM, Gaffard C, Gray MD, Hankers R, Hewison TJ, Kalthoff N, Khodayar S, Kohler M, Kottmeier C, Kraut S, Kunz M, Ladd DN, Lean HW, Lenfant J, Li Z, Marsham J, McGregor J, Mobbs SD, Nicol J, Norton E, Parker DJ, Perry F, Ramatschi M, Ricketts HMA, Roberts NM, Russell A, Schulz H, Slack EC, Vaughan G, Waight J, Watson RJ, Webb AR, Wareing DP, Wieser A. 2007. The Convective Storms Initiation Project. *Bull. Am. Meteorol. Soc.* **88**: 1939–1955.

Bryan GH, Wyngaard JC, Fritsch JM. 2003. Resolution requirements for the simulation of deep moist convection. *Mon. Weather Rev.* **131**: 2394–2416.

Clark PA, Browning KA, Morcrette CJ, Blyth AM, Forbes RM, Brooks B, Perry F. 2013. The evolution of an MCS over southern England. Part 1: Observations. *Q. J. R. Meteorol. Soc.* DOI: 10.1002/qj.2138.

Cotton WR, Alexander GD, Hertenstein R, Walko RL, McAnelly RL, Melville N. 1995. Cloud venting – A review and some new global annual estimates. *Earth Science Rev.* **39**: 169–206.

Cotton WR, Bryan G, van den Heever SC. 2011. *Storm and Cloud Dynamics. International Geophysics* Volume **99**. Elsevier: Amsterdam.

Cram JM, Pielke RA, Cotton WR. 1992. Numerical simulation and analysis of a prefrontal squall line. Part II: Propagation of the squall line as an internal gravity wave. *J. Atmos. Sci.* **49**: 209–225.

Crook NA, Moncrieff MW. 1988. The effect of large-scale convergence on the generation and maintenance of deep moist convection. *J. Atmos. Sci.* **45**: 3606–3624.

Cullen MJP, Davies T, Mawson MH, James JA, Coulter SC, Malcolm A. 1997. An overview of numerical methods for the next generation UK NWP and climate model. In *Numerical Methods in Atmospheric and Ocean Modelling*, the André J. Robert memorial volume. Lin CA, Laprise R, Ritchie H. (eds). Canadian Meteorological and Oceanographic Society: Ottawa. 425–444.

Davies T, Cullen MJP, Malcolm AJ, Mawson MH, Staniforth A, White AA, Wood N. 2005. A new dynamical core for the Met Office's global and regional modelling of the atmosphere. *Q. J. R. Meteorol. Soc.* **131**: 1759–1782.

Droegemeier KK, Wilhelmson RB. 1987. Numerical simulation of thunderstorm outflow dynamics. Part I: Outflow sensitivity experiments and turbulence dynamics. *J. Atmos. Sci.* **44**: 1180–1210.

Essery R, Best M, Cox P. 2001. 'MOSES 2.2 Technical Documentation'. Technical Report No. 30, Hadley Centre: Met Office, Exeter, UK.

Fovell RG, Mullendore GL, Kim S-H. 2006. Discrete propagation in numerically simulated nocturnal squall lines. *Mon. Weather Rev.* **134**: 3735–3752.

Houze RA Jr. 2004. Mesoscale convective systems. *Rev. Geophys.* **42**: RG4003, DOI: 10.1029/2004RG000150.

Gregory D, Rowntree PR. 1990. A mass flux convection scheme with representation of cloud ensemble characteristics and stability-dependent closure. *Mon. Weather Rev.* **118**: 1483–1506.

Lean HW, Clark PA, Dixon M, Fitch A, Forbes R, Halliwell C, Roberts NM. 2008. Characteristics of high-resolution NWP models for forecasting convection over the UK. *Mon. Weather Rev.* **136**: 3408–3424.

Leoncini G, Plant RS, Gray SL, Clark PA. 2009. Perturbation growth at the convective scale for CSIP IOP 18. *Q. J. R. Meteorol. Soc.* **136**: 653–670.

Leoncini G, Plant RS, Gray SL, Clark PA. 2013. Ensemble forecasts of a flood-producing storm: comparison of the influence of model-state perturbations and parameter modifications. *Q. J. R. Meteorol. Soc.* **139**: 198–211.

Lock AP, Brown AR, Bush MR, Martin GM, Smith RNB. 2000. A new boundary-layer mixing scheme. Part 1: Scheme description and single-column model tests. *Mon. Weather Rev.* **128**: 3187–3199.

Ludlam FH. 1980. *Clouds and storms: the behavior and effect of water in the atmosphere*. Pennsylvania State University Press: University Park, PA.

Morrison H. 2012. On the robustness of aerosol effects on an idealized supercell storm simulated with a cloud system-resolving model. *Atmos. Chem. Phys.* **12**: 7689–7705.

Olsson PQ, Cotton WR. 1997. Balanced and unbalanced circulations in a primitive equation simulation of a midlatitude MCC. Part II: Analysis of balance. *J. Atmos. Sci.* **54**: 479–497.

Pandya RE, Durran DR. 1996. The influence of convectively generated thermal forcing on the mesoscale circulation around squall lines. *J. Atmos. Sci.* **53**: 2924–2951.

Parker MD. 2007a. Simulated convective lines with parallel stratiform precipitation. Part I: An archetype for aonvection in along-line shear. *J. Atmos. Sci.* **64**: 267–288.

Parker MD. 2007b. Simulated convective lines with parallel stratiform precipitation. Part II: Governing dynamics and associated sensitivities. *J. Atmos. Sci.* **64**: 289–313.

Parker MD, Johnson RH. 2000. Organizational modes of midlatitude mesoscale convective systems. *Mon. Weather Rev.* **128**: 3413–3436.

Raymond DJ. 1984. A wave–CISK model of squall lines. *J. Atmos. Sci.* **41**: 1946–1958.

Raymond DJ, Jiang H. 1990. A theory for long-lived mesoscale convective systems. *J. Atmos. Sci.* **47**: 3067–3077.

Rotunno R, Klemp JB, Weisman ML. 1988. A theory for strong, long-lived squall lines. *J. Atmos. Sci.* **45**: 463–485.

Schmetz J, Pili P, Tjemkes S, Just D, Kerkmann J, Rota S, Ratier A. 2002. An introduction to Meteosat Second Generation (MSG). *Bull. Amer. Meteorol. Soc.* **83**: 977–992.

Simpson JE. 1987. *Gravity currents in the environment and laboratory*. 2nd ed. Cambridge University Press:Cambridge, UK.

Schmidt JM, Cotton WR. 1990. Interactions between upper and lower tropospheric gravity waves on squall line structure and maintenance. *J. Atmos. Sci.* **47**: 1205–1222.

Schumacher RS. 2009. Mechanisms for quasi-stationary behavior in simulated heavy-rain-producing convective systems. *J. Atmos. Sci.* **66**: 1543–1568.

Thorpe AJ, Miller MJ, Moncrieff MW. 1982. Two-dimensional convection in non-constant shear: A model of midlatitude squall lines. *Q. J. R. Meteorol. Soc.* **108**: 739–762.

Trier SB, Marsham JH, Davis CA, Ahijevych DA. 2011. Numerical simulations of the postsunrise reorganization of a nocturnal mesoscale convective system during 13 June IHOP_2002. *J. Atmos. Sci.* **68**: 2988–3011.

van den Heever SC, Carrio GG, Cotton WR, DeMott PJ, Prenni AJ. 2006. Impacts of nucleating aerosol on Florida storms. Part I: mesoscale simulations. *J. Atmos. Sci.* **63**: 1752–1775.

Weisman ML. 1992. The role of convectively generated rear-inflow jets in the evolution of long-lived mesoconvective systems. *J. Atmos. Sci.* **49**: 1826–1847.

Weisman ML. 2001. Bow echoes: A tribute to TT Fujita. *Bull. Amer. Meteorol. Soc.* **82**: 97–116.

Weisman ML, Skamarock WC, Klemp JB. 1997. The resolution dependence of explicitly modeled convective systems. *Mon. Weather Rev.* **125**: 527–548.

Wilson DR, Ballard SP. 1999. A microphysically based precipitation scheme for the UK Meteorological Office Unified Model. *Q. J. R. Meteorol. Soc.* **125**: 1607–1636.